Perpared for DIS 2002, Krakow

Measurement and NLO DGLAP QCD interpretation of Diffractive Deep Inelastic Scattering

H1 Collaboration

Abstract

A measurement and DGLAP QCD analysis of the inclusive cross section for diffractive deep-inelastic scattering is presented, This corresponds to an extension of the measurement of $F_2^{D(3)}(x_{I\!P}, Q^2, \beta)$ presented in H1prelim-01-111 and uses the same data. The data are now presented in the form of a reduced diffractive cross section $\sigma_r^{D(3)}(x_{I\!P}, Q^2, \beta)$. A new binning scheme is used with fixed values of $x_{I\!P}$, Q^2 and $x = \beta \cdot x_{I\!P}$. These changes facilitate measurements of the ratio of the diffractive to the inclusive DIS cross sections $\sigma_r^{D(3)}(x, Q^2, x_{I\!P})/\sigma_r(x, Q^2)$, which is found to be remarkably flat as a function of Q^2 with $x_{I\!P}$ fixed. A NLO DGLAP QCD fit is performed to the diffractive data and the resulting diffractive parton densities are shown, together with an assessment of the experimental and theoretical uncertainties. The resulting partonic decomposition of the diffractive exchange is dominated by the gluon density, which extends to large fractional momenta. The parton densities are used to make updated comparisons with diffractive dijet and open charm cross sections at HERA and the Tevatron, thus testing QCD hard scattering factorisation as applied to diffraction.

1 Introduction

This document should be taken together with previous H1 results on the inclusive diffractive DIS cross section released for the Budapest conference (H1prelim-01-111) [1]. The measurements presented use the same data and cover essentially the same kinematic range ($Q^2 \geq 6.5\ \mathrm{GeV}^2$, $\beta > 0.01$, $x_{I\!P} < 0.05$). There have been several minor adjustments to the underlying measurement, the only visible changes arising from a modified scattered electron energy cut from $E'_e > 8$ GeV to $E'_e > 6.5$ GeV.

The presentation has now changed in several ways. Firstly, we now work with the 'reduced diffractive cross section' σ_r^D rather than F_2^D, where

$$\sigma_r^D = F_2^D - \frac{y^2}{1 + (1-y)^2}\, F_L^D \ .$$

This is essentially a cosmetic change, since our previous extractions of F_2^D always assumed that the longitudinal diffractive structure function $F_L^D = 0$. However since F_L^D has not yet directly been constrained by data, it is more correct to quote the measurement as a reduced cross section. The NLO QCD fits that follow use σ_r^D as their input.

A new binning scheme is now used, where we work with fixed $x_{I\!P}$ bins (2 per decade) and then study the (x, Q^2) dependence in a binning scheme very similar to that used for the H1 1996-7 low Q^2 F_2 measurement [2]. Since $\beta = x/x_{I\!P}$, β is also always fixed when $x_{I\!P}$ and x are fixed. This binning scheme yields more β bins at fixed x and $x_{I\!P}$ than has previously been possible. It also leads naturally to investigation of the QCD (x, Q^2) or (β, Q^2) structure at fixed $x_{I\!P}$ and to measurements of the ratio of diffractive to inclusive cross sections.

The data are subjected to a DGLAP QCD analysis in order to extract diffractive parton densities for comparisons with hadronic final state measurements. This exercise tests the QCD hard scattering factorisation theorem for semi-inclusive DIS [3]. With the present precision and kinematic range of the data, it is not yet possible to perform these fits at fixed $x_{I\!P}$ and t as would strictly be required by the proof in [3]. Instead we assume a 'Regge factorisation' between the $(x_{I\!P}, t)$ and (β, Q^2) variables, as tested in [1] and use all available data.

2 The Reduced Diffractive Cross Section

Measurements of the recuced diffractive cross section $\sigma_r^{D(3)}(x_{I\!P}, Q^2, x)$, multiplied by $x_{I\!P}$, are presented in detail in figures 1- 7 using the new binning scheme. Figures 1 and 2 show the Q^2 dependence at fixed values of $x_{I\!P}$, x and hence β. Figures 3 and 4 show the x dependence at fixed $x_{I\!P}$ and Q^2. Figures 5 and 6 show the β dependence at fixed $x_{I\!P}$ and Q^2. In each case, the data are compared with the results of the NLO DGLAP QCD fit presented in section 5. For completeness, measurements of $\sigma_r^{D(3)}$ at high Q^2 [4], which are also used in the QCD fits, are shown in figure 7.

3 Summary Plots

To compare the data in a single plot, the diffractive reduced cross section (no additional $x_{I\!P}$ factor) is plotted in fig 8 as a function of β for the $x_{I\!P} = 0.001, 0.003, 0.01$ bins. Figure 9 shows the same thing as a function of x. In figure 10, the Q^2 dependence is shown, including data points from all five $x_{I\!P}$ bins. In figs 11 and 12, the data points from each $x_{I\!P}$ bin are scaled by the assumed values of the 'pomeron flux' in the QCD fits,

$$f_{I\!P/p} = (1/x_{I\!P})^{2\alpha_{I\!P}(0)-1} \int_{-1\ \mathrm{GeV}^2}^{t_{min}} dt\, e^{B_{I\!P} t} ,$$

where the parameters used for the pomeron intercept $\alpha_{I\!P}(0)$ and the $x_{I\!P}$ dependent slope parameter $B_{I\!P}$ are as explained in [1]. No account is taken of possible sub-leading exchange contributions at large $x_{I\!P}$ and small β, though these contributions are small for the data shown ($x_{I\!P} \leq 0.01$). In order to avoid regions which are most likely to be affected by F_L^D, only data with $y < 0.6$ are shown. At LO in QCD, the reduced cross section can then be interpreted in the usual way as a charge weighted sum over the diffractive quark densities. Comparing the data at different values of $x_{I\!P}$ in this way allows the dependences on β and Q^2 to be seen over a wide range. The similarity of the flux-normalised reduced cross sections from different $x_{I\!P}$ values in the overlap regions indicates that the Regge factorisation assumption is a good approximation. In all figures 8- 12, the results of the NLO DGLAP fit to the data (section 5) are also shown.

For $(x, x_{I\!P})$ bins in which there are at least 3 data points, the logarithmic Q^2 derivative, $B = \partial\sigma_r^D/\partial \ln Q^2$ is extracted from fits of the form

$$\sigma_r^D = A(x, x_{I\!P}) + B(x, x_{I\!P}) \ln Q^2 . \tag{1}$$

The results for B from these fits are shown in fig 13. Significant scaling violations with positive $\partial\sigma_r^D/\partial \ln Q^2$ persist up to large values of $\beta \sim 0.7$, with a change in this behaviour for the highest β values. The logarithmic Q^2 derivative is sensitive to the diffractive gluon density, which is required by the data to remain large up to high values of β. The behaviour is once again similar at the different values of $x_{I\!P}$.

4 Diffractive to Inclusive Cross Section Ratio

The ratio of σ_r^D to the inclusive reduced cross section σ_r is formed by dividing $\sigma_r^D(x_{I\!P}, x, Q^2)$ in each $x_{I\!P}$ bin by the measured $\sigma_r(x, Q^2)$, as obtained in [2]. The ratio as a function of Q^2 tests the difference between the scaling violations of σ_r^D and σ_r when compared at the same x. This ratio is shown separately for each $x_{I\!P}$ and x bin in figure 14 and in a single plot for all $x_{I\!P}$ bins in figure 15. At low values of β, the ratio is remarkably flat as a function of Q^2 for all $x_{I\!P}$ values. At the highest β, the ratio falls with increasing Q^2.

In order to quantify the differences between the Q^2 dependences of σ_r^D and σ_r, the logarithmic derivative of the ratio is obtained, corresponding to parameter B in fits of the form

$$\sigma_r^D/\sigma_r = A + B \ln Q^2 ,$$

such that

$$B = \frac{\partial}{\partial \ln Q^2} \left(\sigma_r^D/\sigma_r\right) \ . \tag{2}$$

The fits to the data are shown in figures 14 and 15. The resulting values of B are shown in fig 16. Once again, the 'pomeron flux' at fixed $x_{I\!P}$ is divided out, so that the results at different $x_{I\!P}$ can be compared in normalisation as well as shape.

The ratio as a function of x with Q^2 and $x_{I\!P}$ fixed is shown in fig 17. In each figure, dashed lines indicate the point in x at which $\beta = 1$ ($x = x_{I\!P}$). Dotted lines indicate the point where $\beta = 0.1$ ($x = 0.1 \cdot x_{I\!P}$). For $\beta > 0.1$, a complicated structure is observed in the ratio, corresponding to the high β behaviour of σ_r^D (see figs 5, 6 and 8). For $\beta < 0.1$, there is a suggestion that a flatter dependence develops, though there are limited data in this region.

It should be noted that the diffractive to inclusive ratios as presented here must be interpreted slightly differently to those shown by H1 in [1] as[1] $\rho^{D(3)}$ and by ZEUS [5]. In the two former cases, β and Q^2 (hence also $M_{\rm X}$) are held fixed as x (or W) varies. In the present work, $x_{I\!P}$ and Q^2 are held fixed as x varies, such that $M_{\rm X}$ also varies with x.

5 NLO DGLAP QCD Fits

Both LO and NLO QCD fits have been performed to σ_r^D in the $(\beta, Q^2, x_{I\!P})$ binning scheme (see [1]). It is assumed that the diffractive parton densities vary only in normalisation with $x_{I\!P}$ and t and the dependence on these variables is parameterised using the Regge flux factor $f_{I\!P/p}$ as in the 'Regge' fits from [1], with $\alpha_{I\!P}(0) = 1.173$. The massive scheme is used for heavy quarks. The LO fit is subject to the restrictions $y < 0.45$ and $M_{\rm X} > 2$ GeV in order to avoid regions that are most likely to be influenced by F_L^D or where significant higher twist contributions may be present. For the NLO fit, where the effects of F_L^D are considered through its relation to the NLO gluon density, the only cut is $M_{\rm X} > 2$ GeV. No explicit β cut is made in either fit.

Using a modified version of the fitting code used for F_2 in [2] (Pascaud, Zomer), it has been possible for the first time to asign experimental errors to the extracted parton densities, including a full propagation of all systematic uncertainties considered in the measurement. In addition, theoretical uncertainties corresponding to $\Lambda = 200 \pm 30$ MeV, $m_c = 1.5 \pm 0.1$ GeV and all assumed parameters for the pomeron and meson flux (uncertainties as in [1]) have been evaluated. High Q2 H1 data points [4] are also included in the fits, their systematic uncertainties taken to be fully uncorrelated.

The data in the new $(x, Q^2, x_{I\!P})$ binning scheme are compared with the predictions of the NLO QCD fit in figs 1- 12. The extracted NLO singlet-quark and gluon parton densities, together with their uncertainties are shown in figures 18 and 19. For comparison, the central result from the LO fit is also shown. In these figures, the variable z corresponds to the momentum fraction carried by an individual parton ($z = \beta$ for quarks, $z > \beta$ for gluons). In figure 20, the results are compared with the results of a previous H1 LO fit using earlier data [6]. Figure 21

[1]Note that $\rho^{D(3)}$ was found to vary little with W (or x) with Q^2 and β (hence $M_{\rm X}$) held fixed in [1].

shows the fraction of the total exchanged longitudinal momentum that is carried by gluons, integrated over the measured kinematic range $0.01 < z < 1$. This fraction is approximately $75 \pm 15\%$, relatively constant with Q^2. Figure 22 shows the leading twist component of F_L^D as predicted from the fits through its relation to the NLO gluon density.

6 Comparisons with hadronic Final State Observables

The partons extracted from the LO QCD fits have been implemented in the RAPGAP Monte Carlo generator and used to make predictions for various hadronic final state observables. The results are shown for the H1 diffractive jets measurements [7] in figs 23- 28 and for the H1 diffractive D^* measurements [8] in figs 29- 30. The new predictions based on σ_r^D are in better agreement with the charm data was previously the case based on the partons from [6]. The agreement with the dijet data is not as good as that using the partons from [6]. Taking account of the considerable uncertainties in the parton densities, final state modelling uncertainties and undetermined higher order QCD effects, the data remain in agreement with hard scattering factorisation as proven for semi-inclusive DIS [3].

A comparison of predictions using the extracted partons densities with the quantity $\tilde{F}_{JJ}^D(\beta)$ as measured by the CDF collaboration [9] is shown in figure 31. The new prediction is slightly closer to the data than that using the partons extracted in [6], though a discrepancy at the level of an order of magnitude remains. This has often been interpreted as evidence for absorptive corrections in diffractive hadron-hadron scattering (rapidity gap survival probabilities). The comparison with the newly obtained parton densities suggests that the gap survival probability may be less dependent on β than was previously thought.

7 Summary

The inclusive cross section for diffractive DIS has been presented in a modified way, allowing closer inspection of the β and Q^2 dependences at fixed values of the fractional loss of longitudinal momentum of the proton during the interaction, $1 - x_{\mathbb{P}}$. The data are presented in ways that are directly sensitive to the shapes of the diffractive singlet-quark and gluon densities. These illustrations confirm the need for a dominant gluon density in diffration, extending to large fractional momenta.

The x and Q^2 dependences of the ratio of the diffractive to the inclusive DIS cross sections has been presented for fixed $x_{\mathbb{P}}$ values. The Q^2 dependence of this ratio is remarkably small over a large kinematic region.

New parton densities describing diffractive DIS have been extracted from NLO DGLAP QCD fits to the data. For the first time, it has been possible to ascribe experimental and theoretical errors to these parton densities. The results are broadly in line with a previous result from H1, though the magnitude of the gluon density is somewhat smaller in the new version. Approximately 75% of the total exchanged momentum is carried by gluons.

The parton densities have been used to make updated comparisons with hadronic final state data assuming QCD hard scattering factorisation. The predictions for lepton proton scattering remain consistent with the final state measurements, whilst large additional gap survival probabilities continue to be necessary to obtain a good description of $p\bar{p}$ data from the Tevatron.

References

[1] H1 Collaboration, *'Measurement of the diffractive structure function $F_2^{D(3)}$'*. Paper submitted to International Europhysics Conference on High Energy Physics EPS01, Budapest, July 2001 (abstract 808). Available from http://www-h1.desy.de/h1/www/publications/htmlsplit/H1prelim-01-111.long.html

[2] H1 Collaboration, C. Adloff *et al.*, *Eur. Phys. J.* **C 21** (2001) 33.

[3] J. Collins, *Phys. Rev.* **D 57** (1998) 3051 and erratum-ibid. **D 61** (2000) 019902.

[4] H1 Collaboration, *Measurement and Interpretation of the Diffractive Structure Function $F_2^{D(3)}$ at HERA*. Paper submitted to International Conference on High Energy Physics ICHEP98, Vancouver, July 1998 (abstract 571).

[5] ZEUS Collaboration, J. Breitweg *et al.*, *Eur. Phys. J.* **C 6** (1999) 43.
ZEUS Collaboration, S. Chekanov et al., DESY-02-029, submitted to Eur. Phys. Journal C.

[6] H1 Collaboration, C. Adloff *et al.*, *Z. Phys.* **C 76** (1997) 613.

[7] H1 Collaboration, C. Adloff *et al.*, *Eur. Phys. J.* **C 20** (2001) 29.

[8] H1 Collaboration, C. Adloff *et al.*, *Phys. Lett.* **B 520** (2001) 191.

[9] CDF Collaboration, T. Affolder *et al.*, *Phys. Rev. Lett.* **84** (2000) 5043.

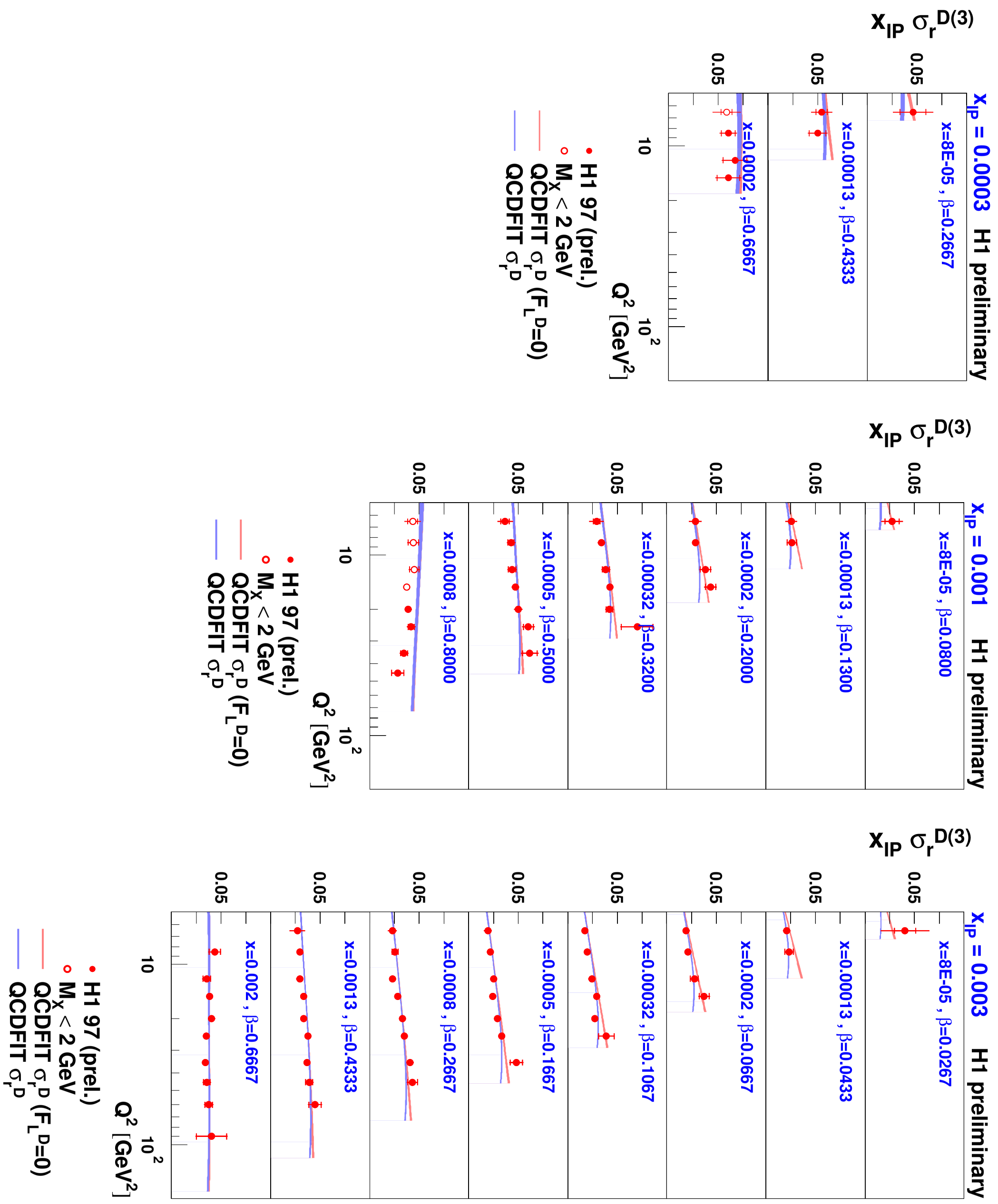

Figure 1: Reduced diffractive cross section data for fixed $x_{I\!P} = 0.0003, 0.001, 0.003$ and fixed x, shown as a function of Q^2 and compared with the results of the NLO QCD fit (experimental errors only). The filled data points were included in the fit. The open data points ($M_{\rm X} < 2\,{\rm GeV}$) were omitted. The predictions of the NLO fit for F_2^D (i.e. σ_r^D for $F_L^D = 0$) are also shown. Rising scaling violations are observed except at the highest β.

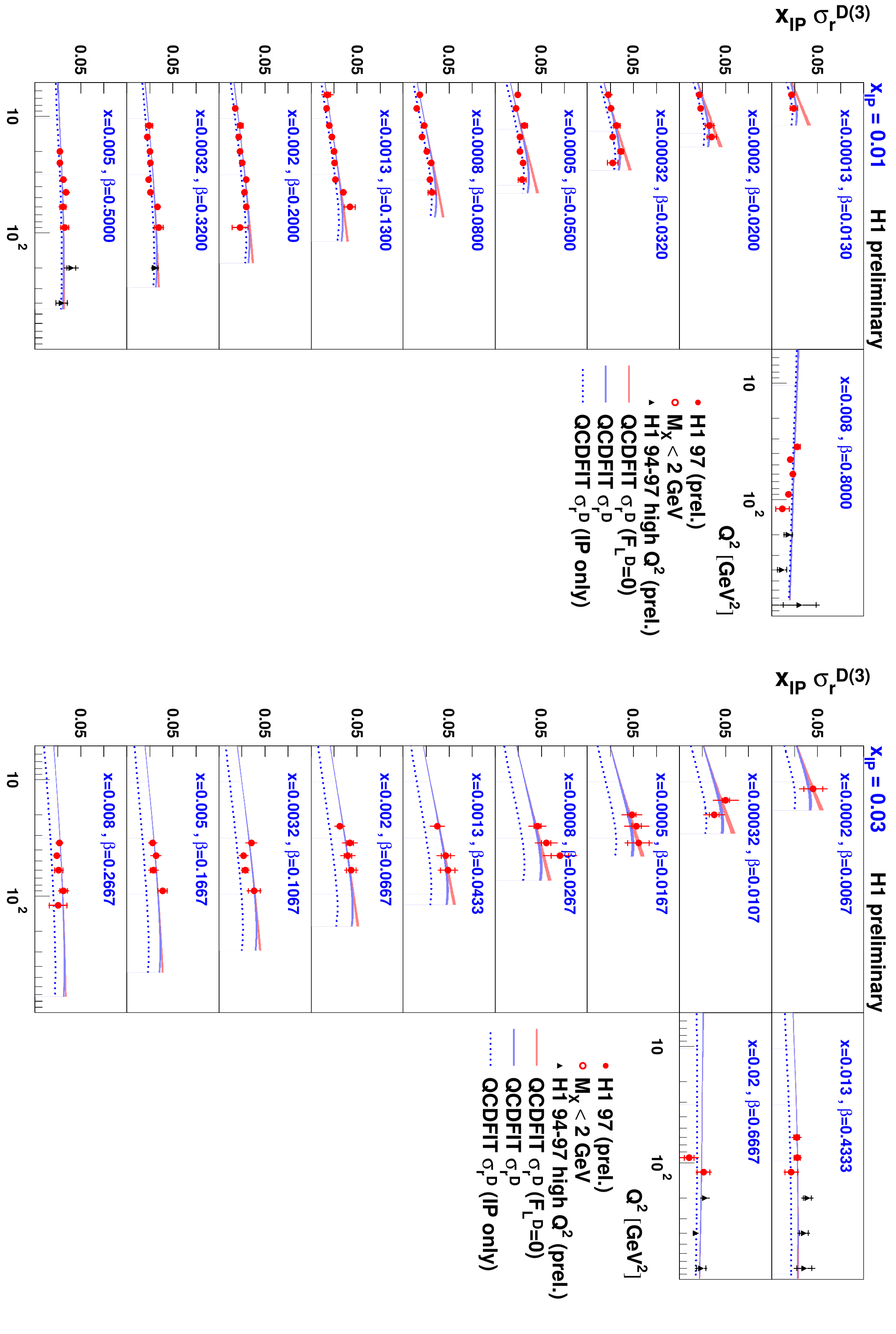

Figure 2: Reduced diffractive cross section data for fixed $x_{I\!P} = 0.01, 0.03$ and fixed x, shown as a function of Q^2 and compared with the results of the NLO QCD fit. The contribution to the predicted reduced cross section from the leading 'pomeron' term alone is also shown (the remainder being asigned to sub-leading meson exchange).

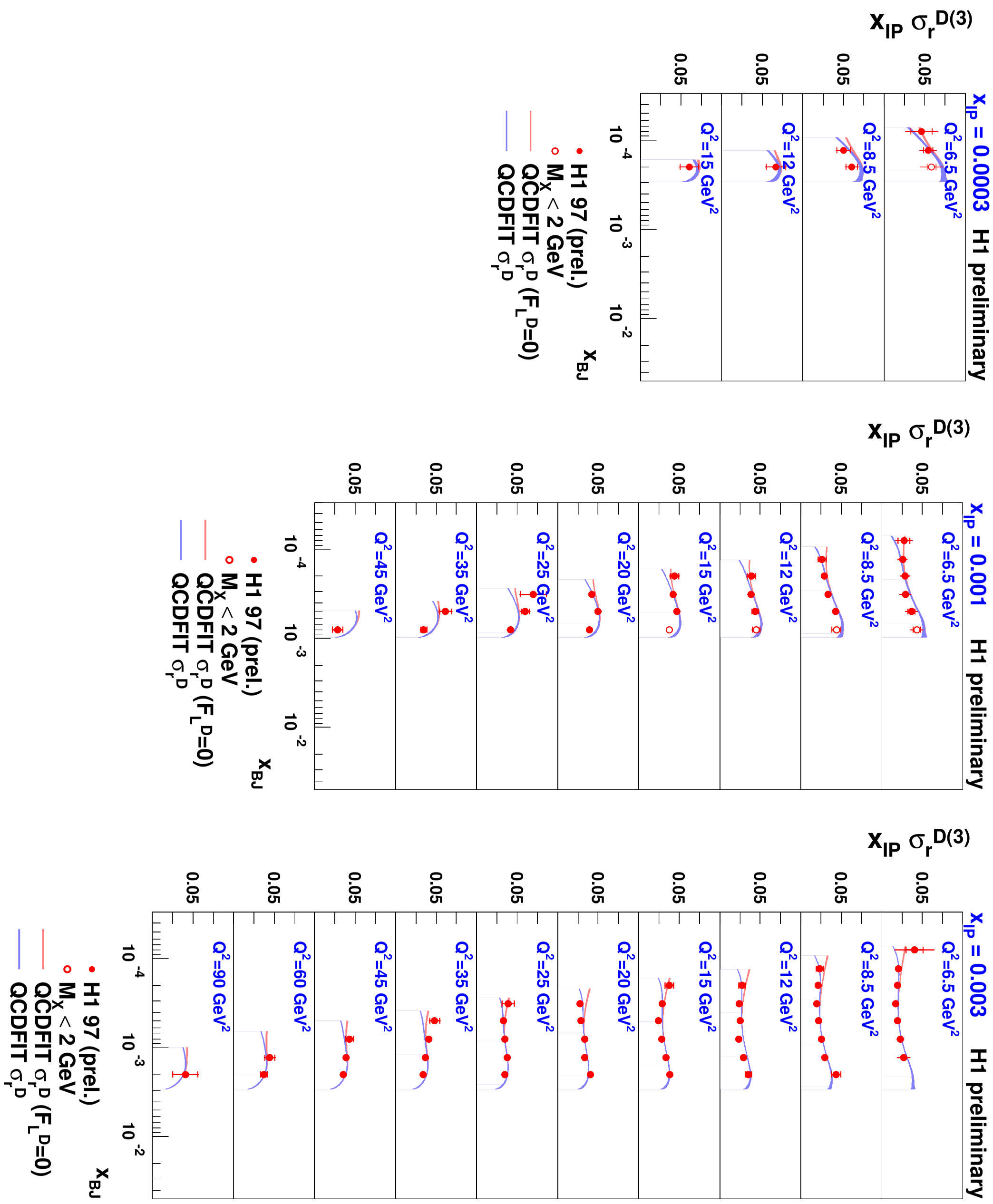

Figure 3: Reduced diffractive cross section data for fixed $x_{I\!P} = 0.0003, 0.001, 0.003$ and fixed Q^2, shown as a function of x and compared with the results of the NLO QCD fit. The shape of the distributions at fixed Q^2 varies with $x_{I\!P}$, since different regions of β are probed for the different $x_{I\!P}$ values. Note that the cross section is constrained to tend to zero as $x \to x_{I\!P}$ ($\beta \to 1$).

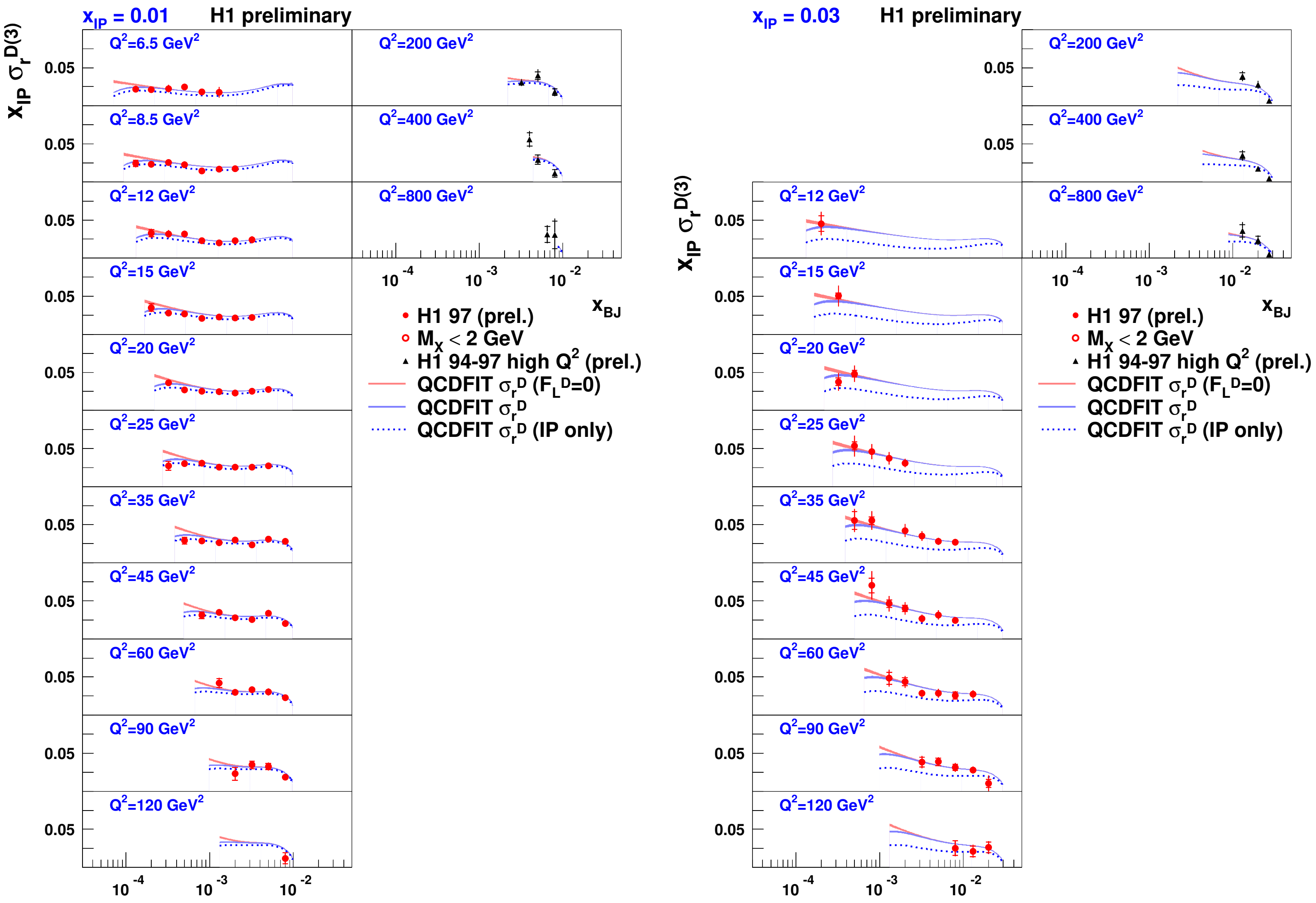

Figure 4: Reduced diffractive cross section data for fixed $x_{I\!P} = 0.01, 0.03$ and fixed Q^2, shown as a function of x and compared with the results of the NLO QCD fit.

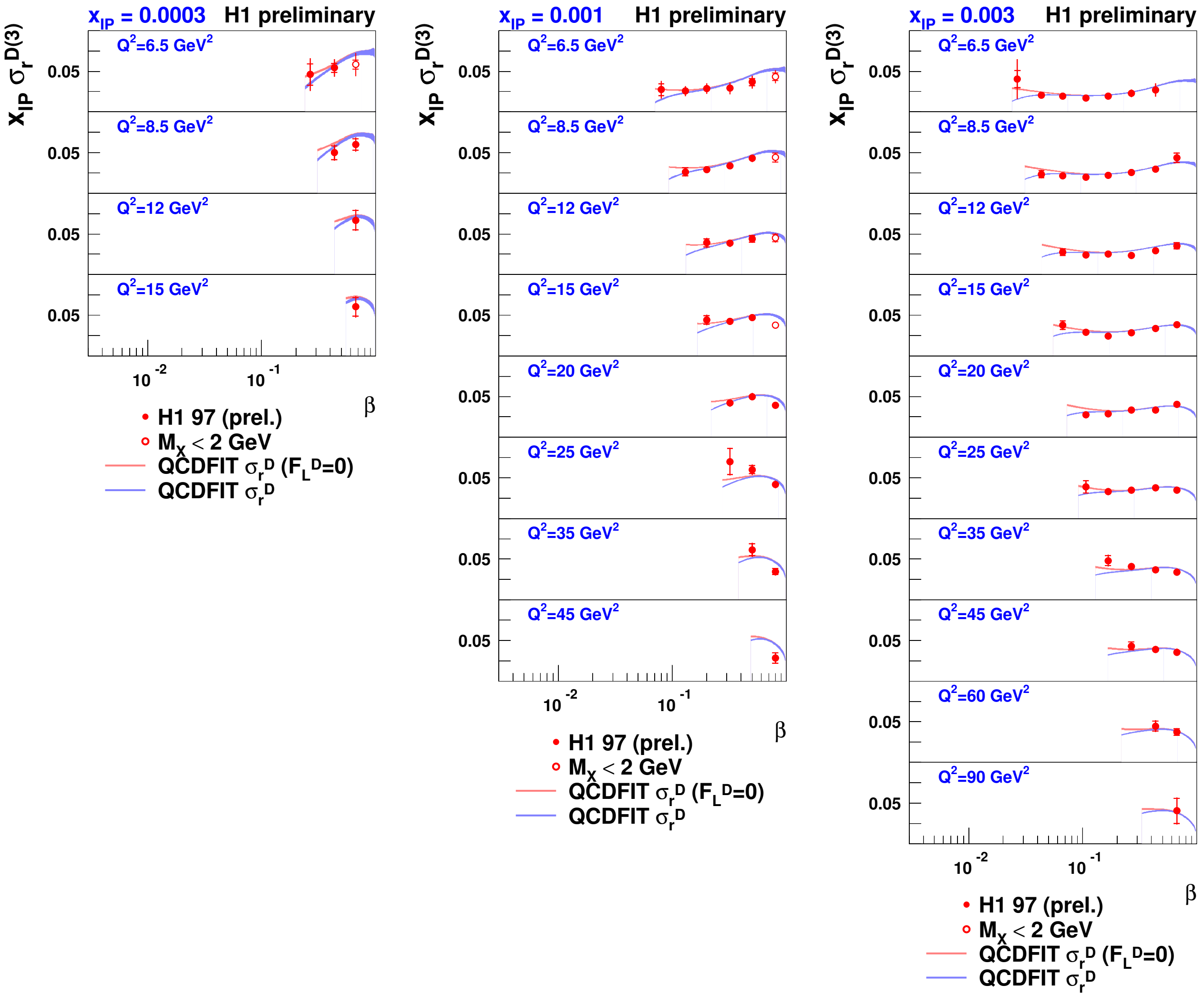

Figure 5: Reduced diffractive cross section data for fixed $x_{I\!P} = 0.0003, 0.001, 0.003$ and fixed Q^2, shown as a function of β and compared with the results of the NLO QCD fit. The shape of the distributions at fixed Q^2 is similar for different $x_{I\!P}$ values.

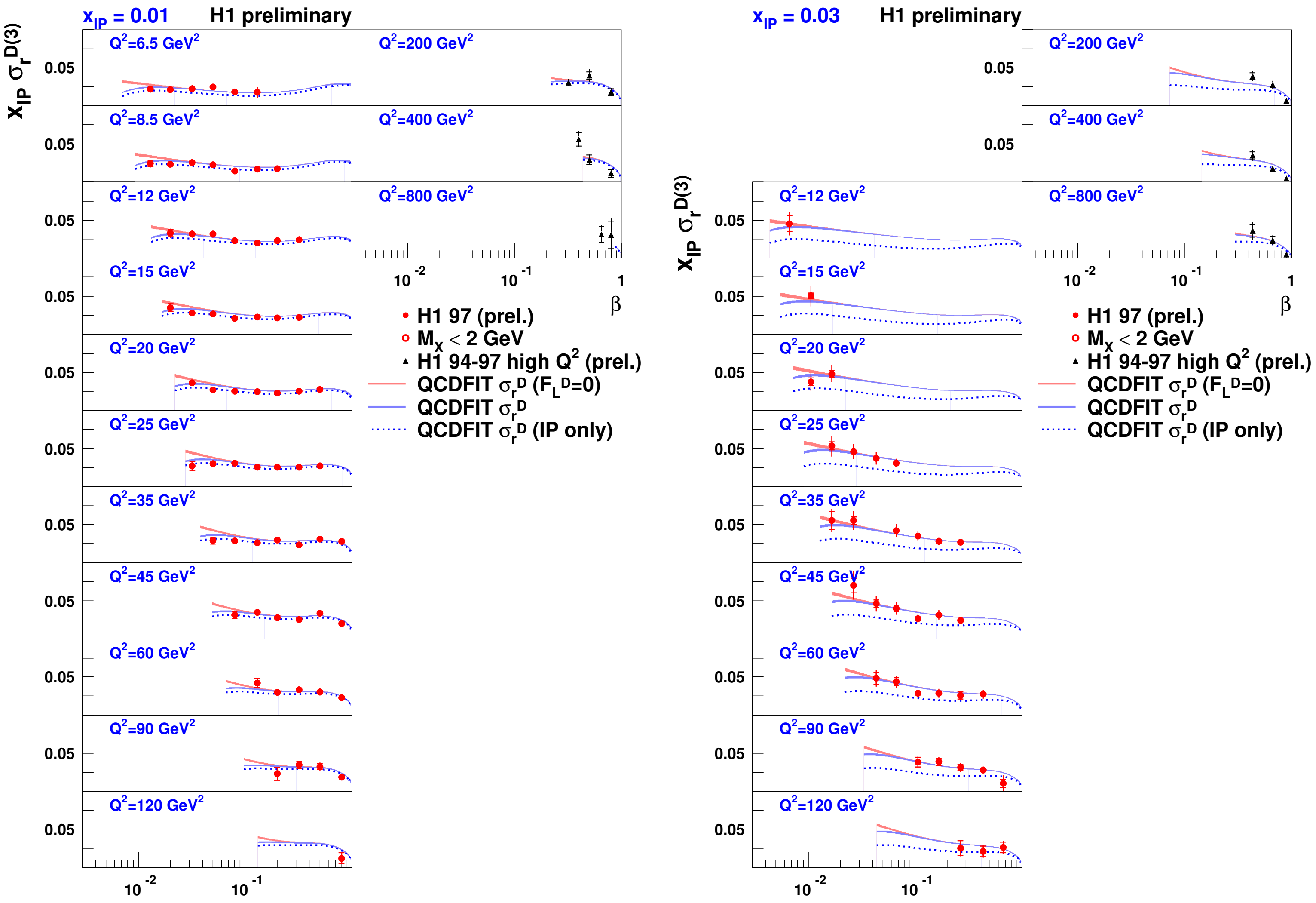

Figure 6: Reduced diffractive cross section data for fixed $x_{I\!P} = 0.01, 0.03$ and fixed Q^2, shown as a function of β and compared with the results of the NLO QCD fit.

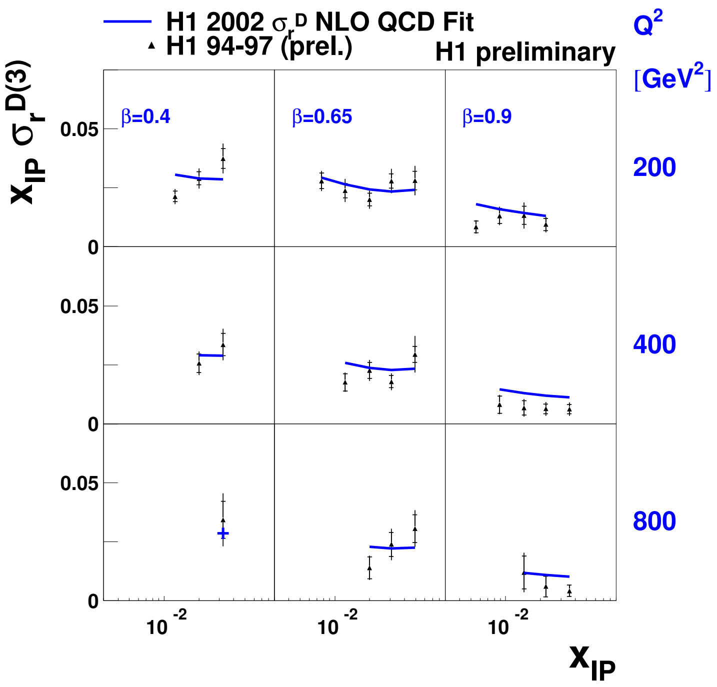

Figure 7: High Q^2 data as released for the Vancouver ICHEP conference (1998) [4] compared with the predictions of the QCD fit.

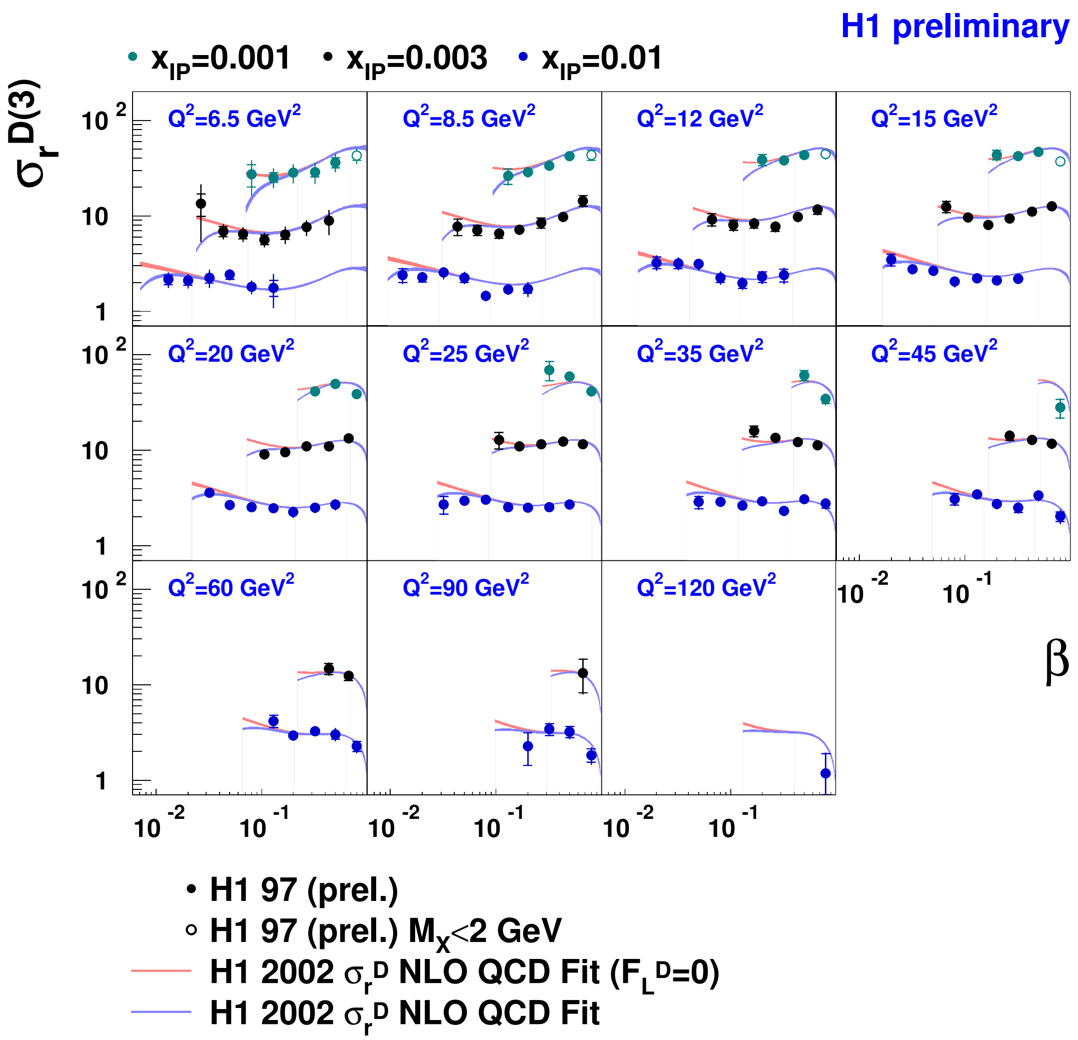

Figure 8: β dependence of the reduced cross section at fixed $x_{I\!P} = 0.001, 0.003, 0.01$ and fixed Q^2, compared with the predictions of the NLO QCD fit.

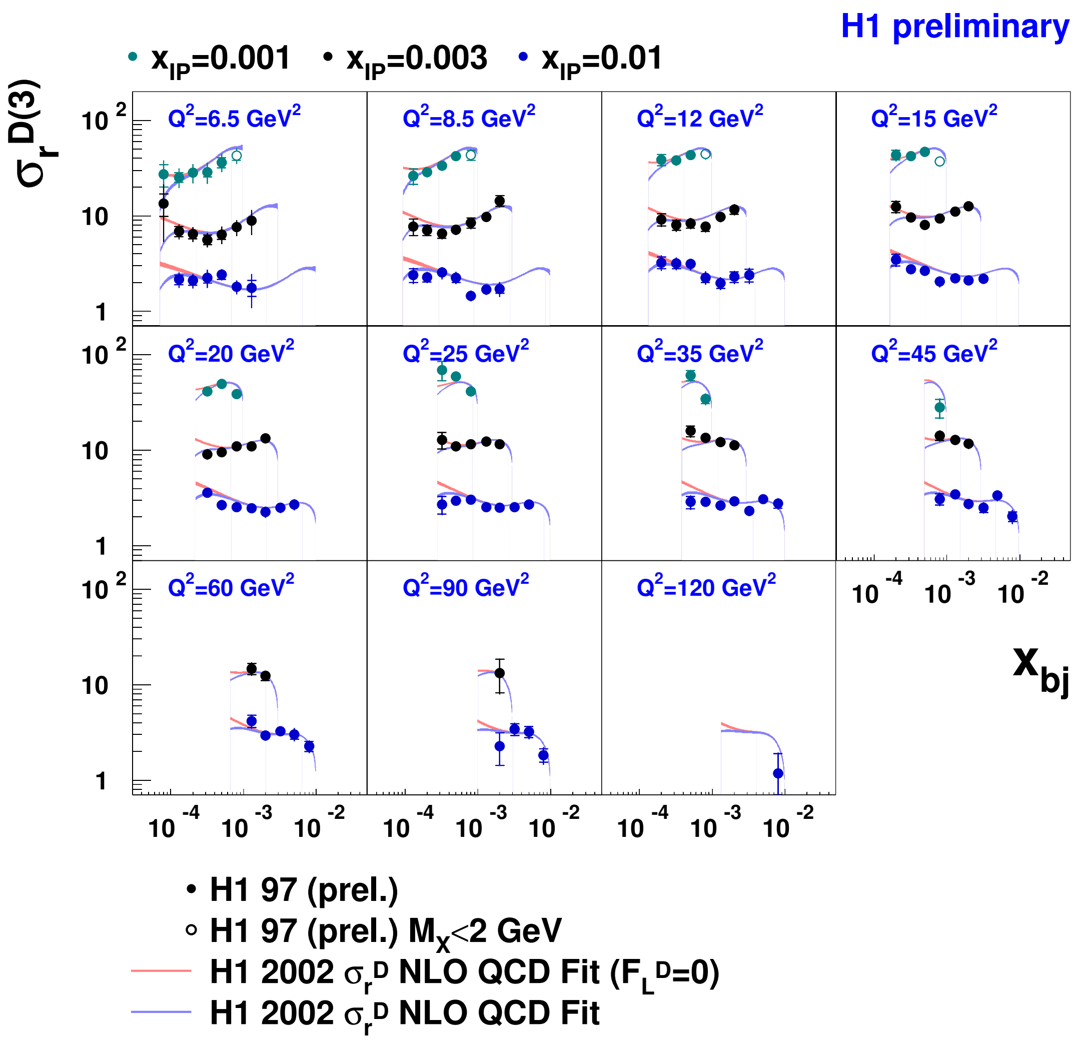

Figure 9: x dependence of the reduced cross section at fixed $x_{I\!P} = 0.001, 0.003, 0.01$ and fixed Q^2, compared with the predictions of the NLO QCD fit.

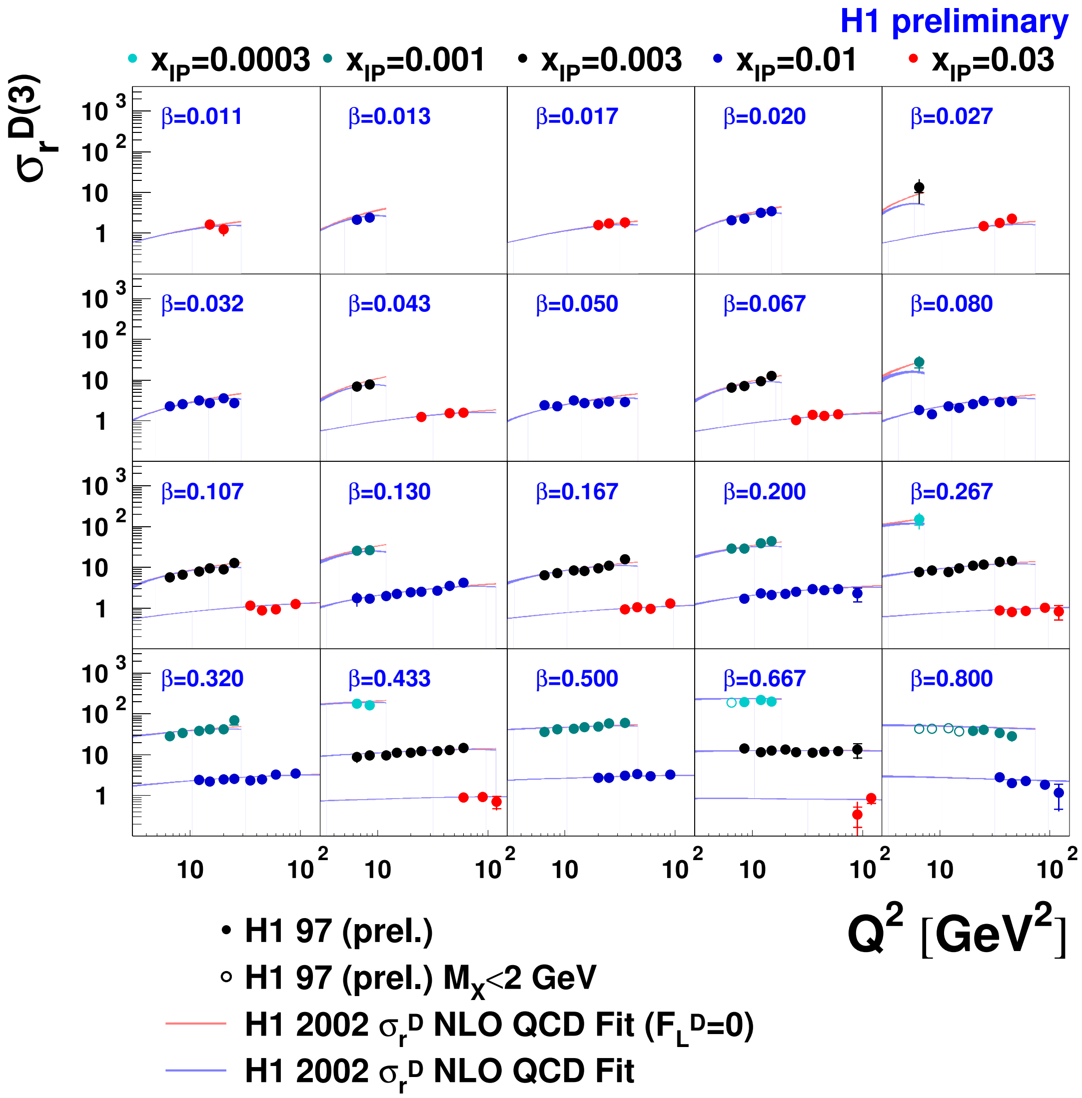

Figure 10: Q^2 dependence of the reduced cross section at fixed $x_{I\!P} = 0.0003, 0.001, 0.003, 0.01, 0.03$ and fixed x, compared with the predictions of the NLO QCD fit.

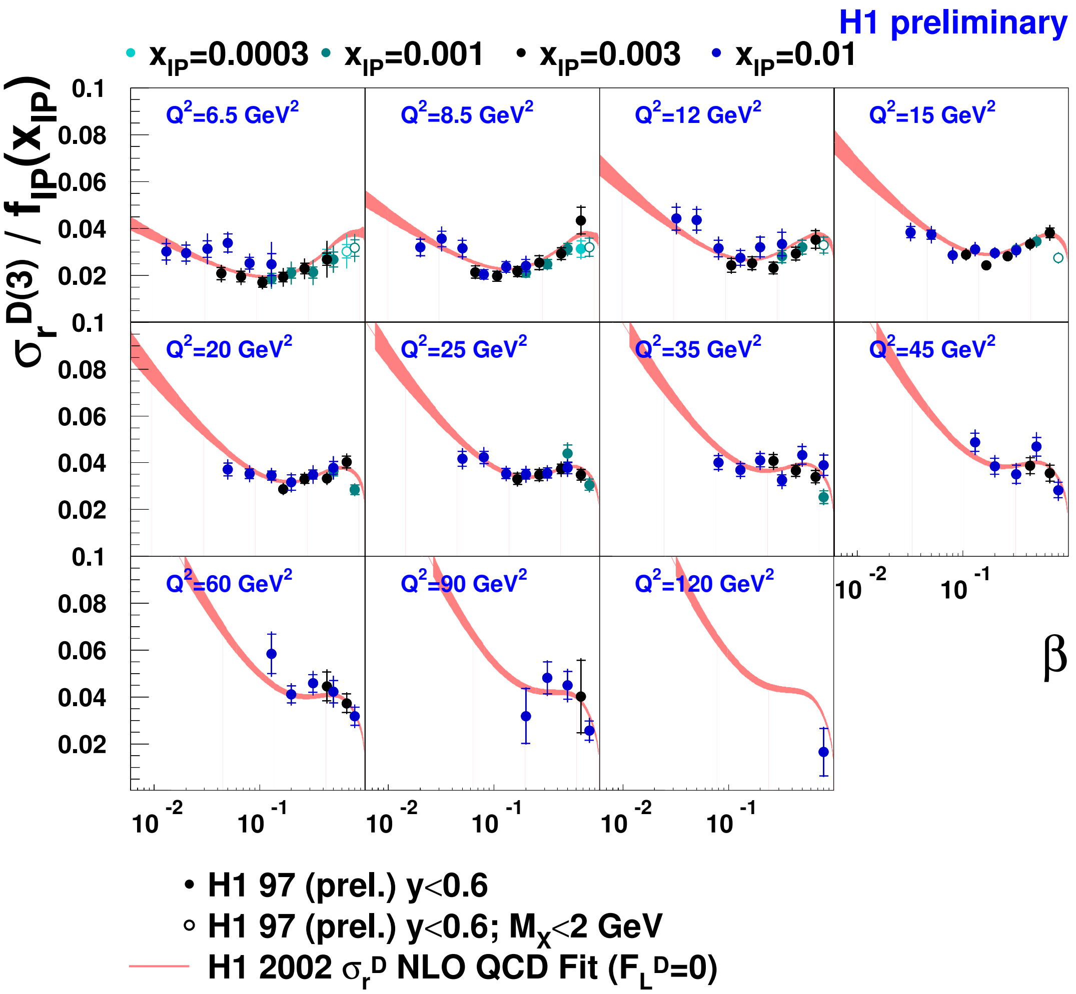

Figure 11: β dependence of the reduced cross section scaled at each $x_{I\!P}$ by the values assumed for the t-integrated pomeron flux in the QCD fits. Only data with $y < 0.6$ are shown. The data are compared with the prediction of the NLO QCD fits (experimental errors only). Since the different $x_{I\!P}$ bins are sensitive to different regions of β, comparing $x_{I\!P}$ bins in this way shows the shape of the singlet density extracted in the fits directly from the data. Although the pomeron flux factor is used here primarily as a convenient parameterisation of the $x_{I\!P}$ dependence, the level of agreement between the data and the QCD fit also indicates the extent to which the Regge factorisation hypothesis is valid.

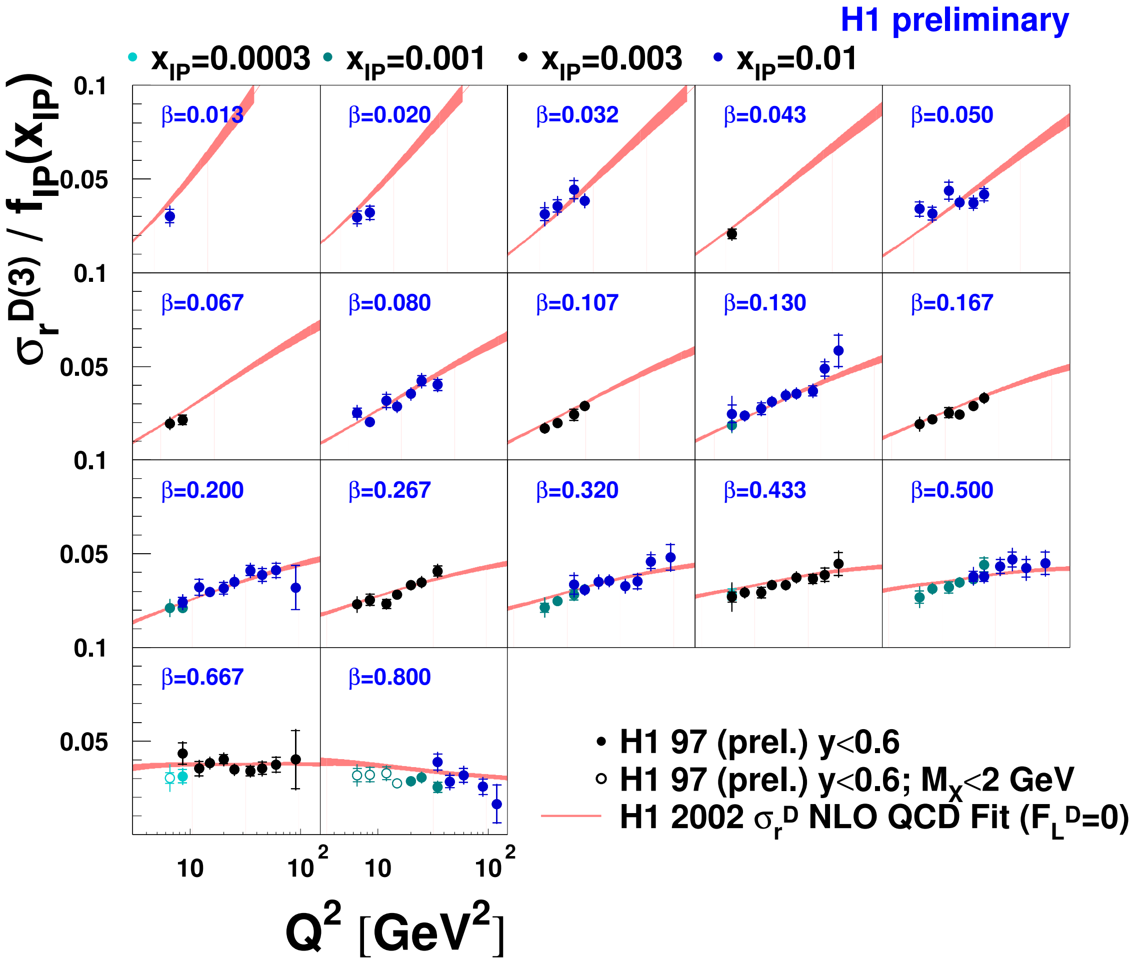

Figure 12: Q^2 dependence of the reduced cross section ($y < 0.6$) scaled at each $x_{I\!P}$ by the values assumed for the t-integrated pomeron flux in the QCD fits. The data are compared with the prediction of the NLO QCD fits (experimental errors only).

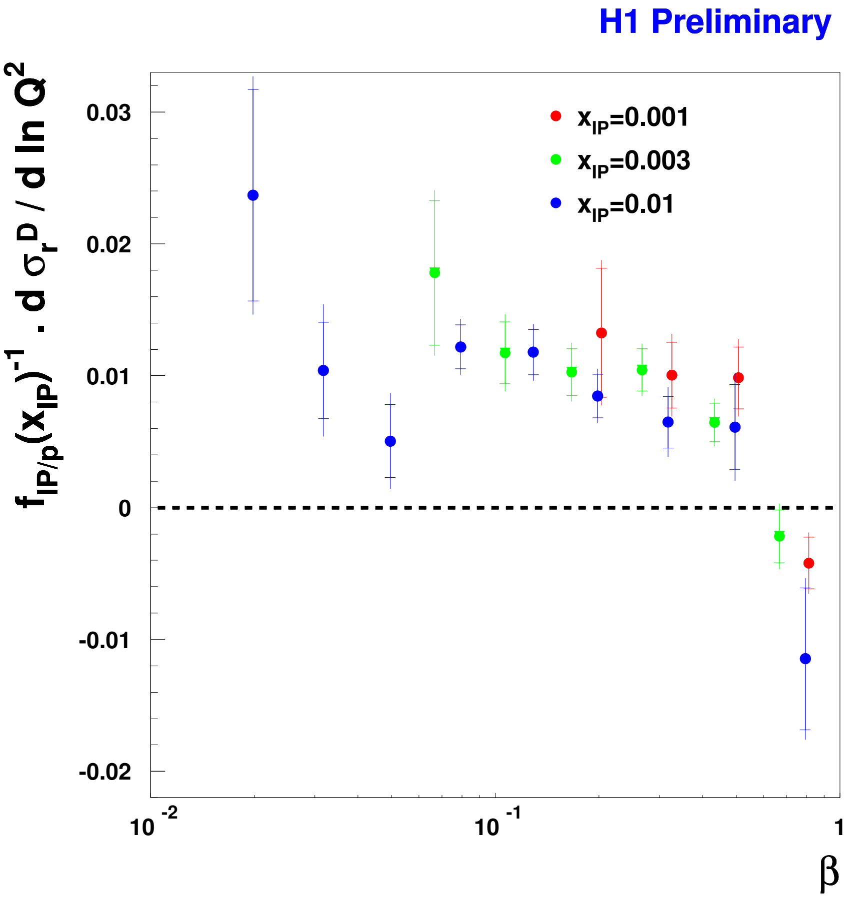

Figure 13: Logarithmic Q^2 derivatives of σ_r^D for different β and $x_{I\!P}$, scaled at each $x_{I\!P}$ by the values assumed for the t-integrated pomeron flux in the QCD fits. The plot shows that the scaling violations of σ_r^D remain positive up to high values of $\beta \sim 0.7$, but become negative at the highest β. The scaling violations at fixed β are very similar at the different $x_{I\!P}$ values, as expected in Regge factorisation models. The logarithmic Q^2 dependence is sensitive to the LO diffractive gluon density convoluted with α_s and the splitting function P_{qg}. Care about kinematic correlations between β and Q^2 has to be taken in this interpretation, though the data are all in the pQCD region ($Q^2 \geq 6.5\ \mathrm{GeV}^2$) and there is no evidence for changes in the results with $x_{I\!P}$, which might be expected since the difference $x_{I\!P}$ bins cover different Q^2 regions.

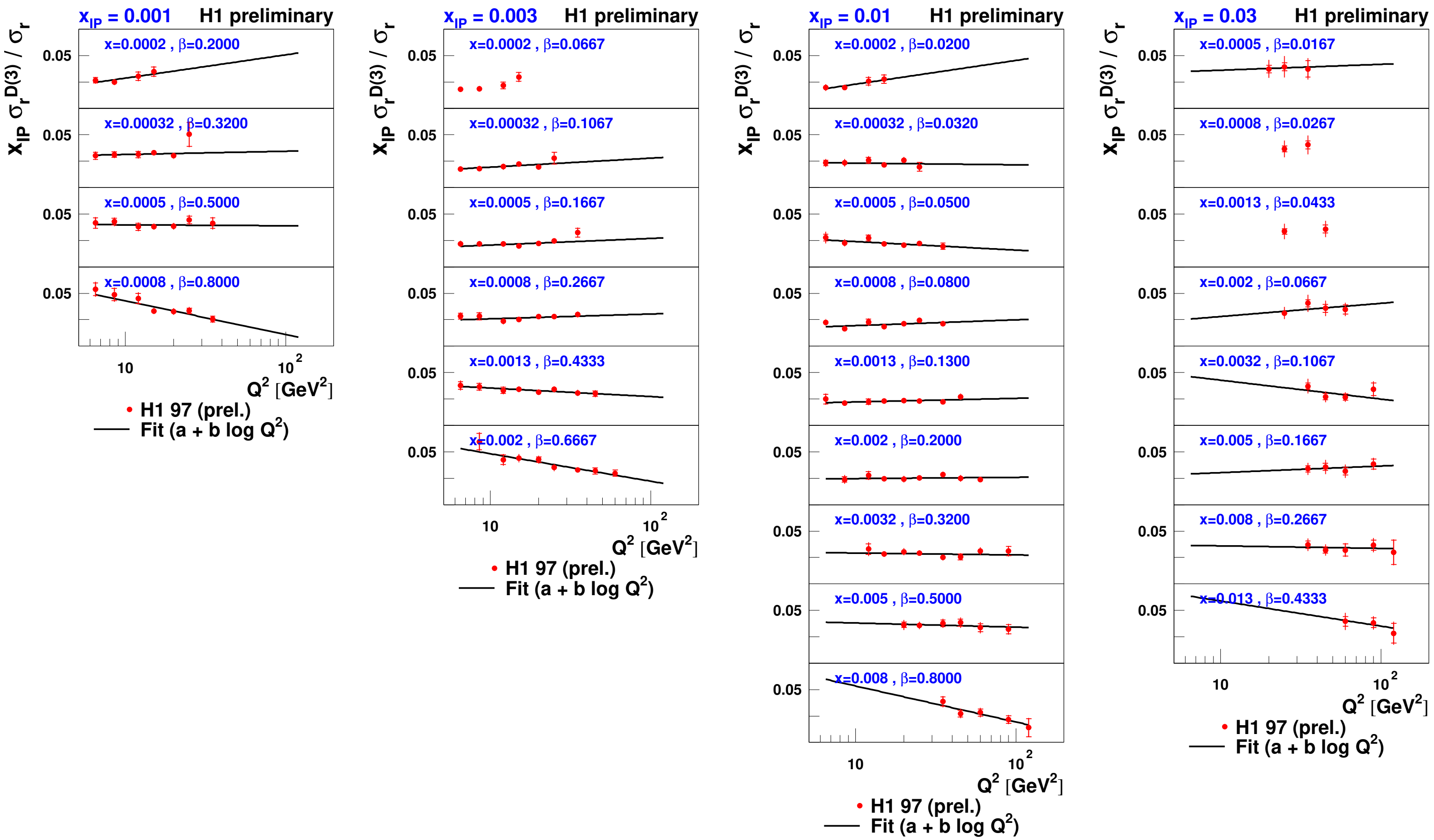

Figure 14: The ratio of diffractive to the inclusive reduced cross section, shown as a function of Q^2 in different $x_{I\!P}$ and x bins. The results of the fit to a logarithmic Q^2 dependence are overlaid. The Q^2 dependence of the ratio is small except at the highest β and varies little with $x_{I\!P}$.

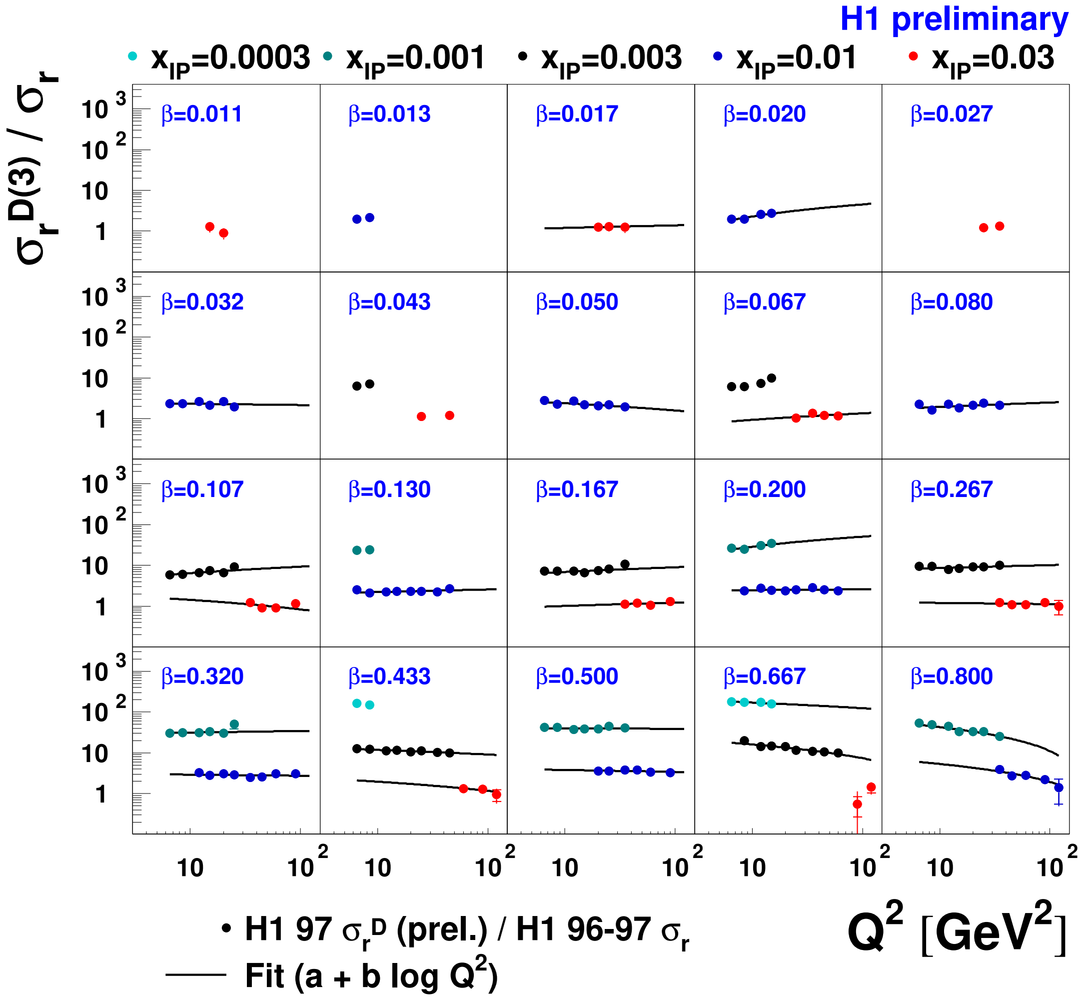

Figure 15: The ratio of diffractive to inclusive reduced cross sections, shown as a function of Q^2. The results of the fit to a logarithmic Q^2 dependence are overlaid. The Q^2 dependence of the ratio is small for most β and varies little with $x_{I\!P}$.

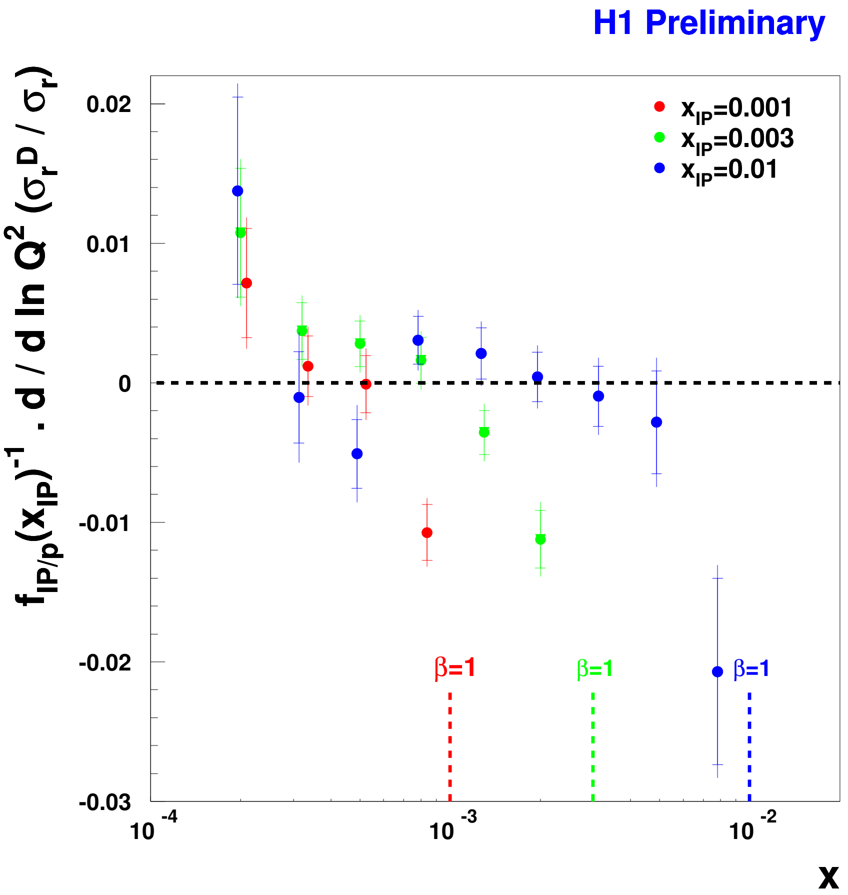

Figure 16: Logarithmic Q^2 derivatives of the ratio σ_r^D/σ_r, the $x_{\mathbb{P}}$ dependence of σ_r^D having been divided out using a parameterisation of the 'pomeron' flux. The data are consistent with identical Q^2 dependences of the diffractive and inclusive cross sections away from $\beta = 1$, with clear differences from this behaviour as $\beta \rightarrow 1$.

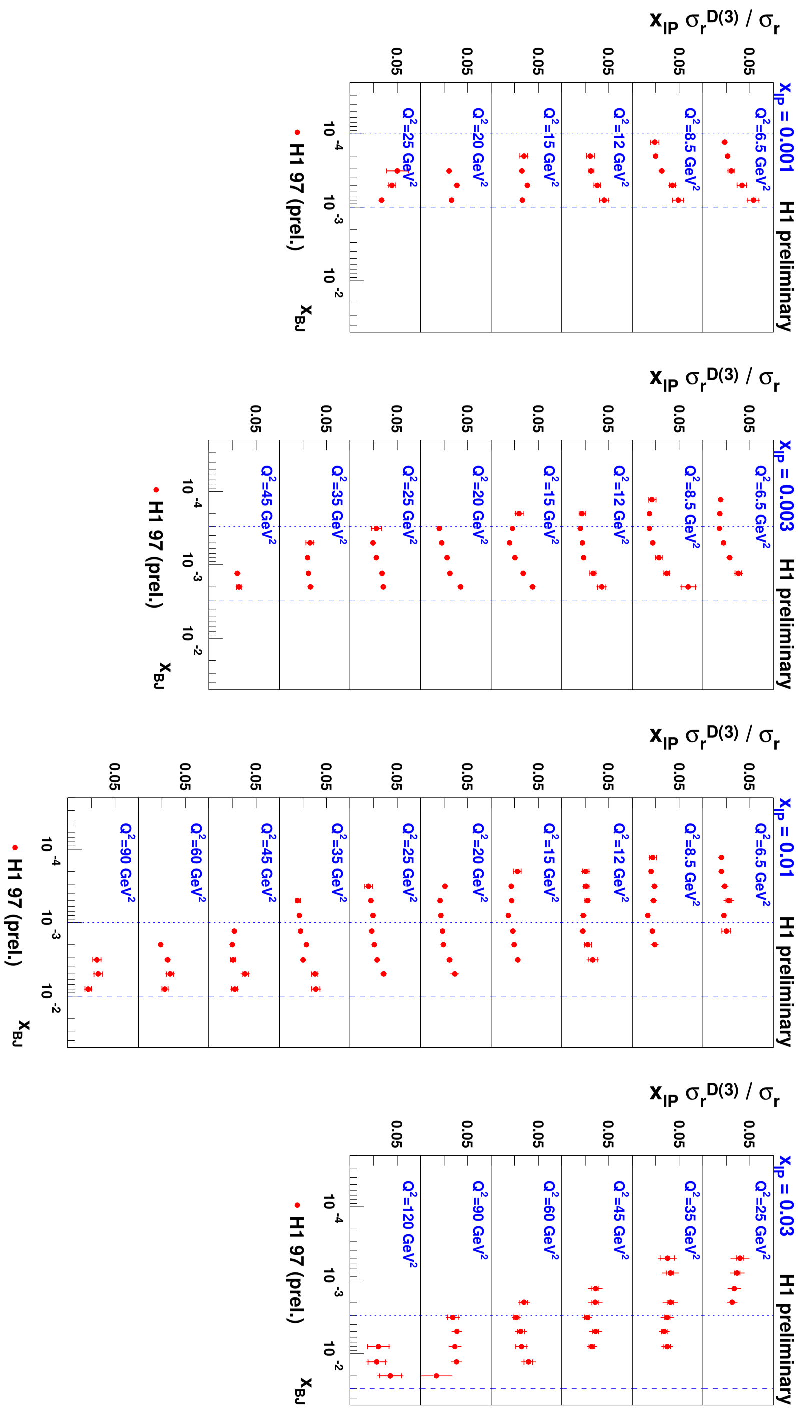

Figure 17: The ratio of diffractive to inclusive reduced cross sections, shown as a function of x at fixed $x_{I\!P}$ and Q^2 values. Note that $M_X^2 = Q^2(x_{I\!P}/x - 1)$ varies with x in these plots. The dashed (dotted) lines indicate the points at which $\beta = 1$ ($\beta = 0.1$). Clear variations in the shape are observed for the different $x_{I\!P}$ values, arising from the fact that they cover different β ranges. For the high β region, the ratio has a complicated shape, since the structure of σ_r^D is rather complicated in this region, whereas σ_r is well parameterised by $x^{-\lambda}$. For the lowest β, a flatter dependence of the ratio on x is observed.

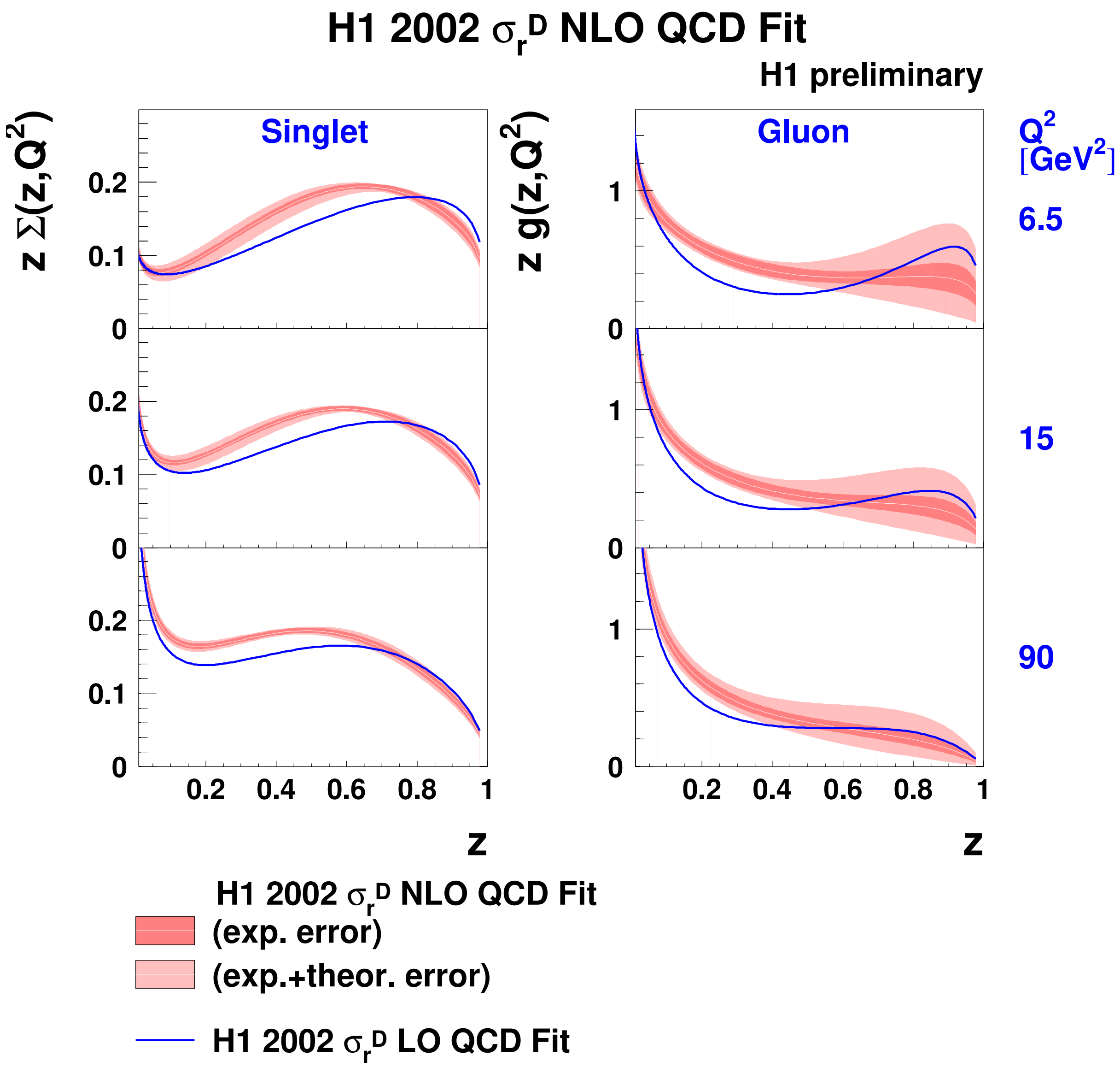

Figure 18: Diffractive parton densities normalised such that the 'pomeron flux' is unity at $x_{I\!P} = 0.003$. The left hand side shows the singlet quark distribution ($6 * u$ where we assume $u = d = s = \bar{u} = \bar{d} = \bar{s}$). The right hand side shows the gluon density. The red bands show the results of the NLO fits, with inner error bands showing the experimental errors (statistical and systematic) and the outer errors bands showing the full uncertainties, including those arising from theoretical assumptions. For comparison, the central values of the parton densities extracted from the LO fit are also shown (blue line). The LO gluon density shows a peak at the highest z. This peak disappears for the central values when moving to NLO, an effect which is due to the different theory rather than the extra high β data in the NLO fit. The uncertainties in this region remain large. At smaller z, the relative size of the uncertainties is significantly reduced.

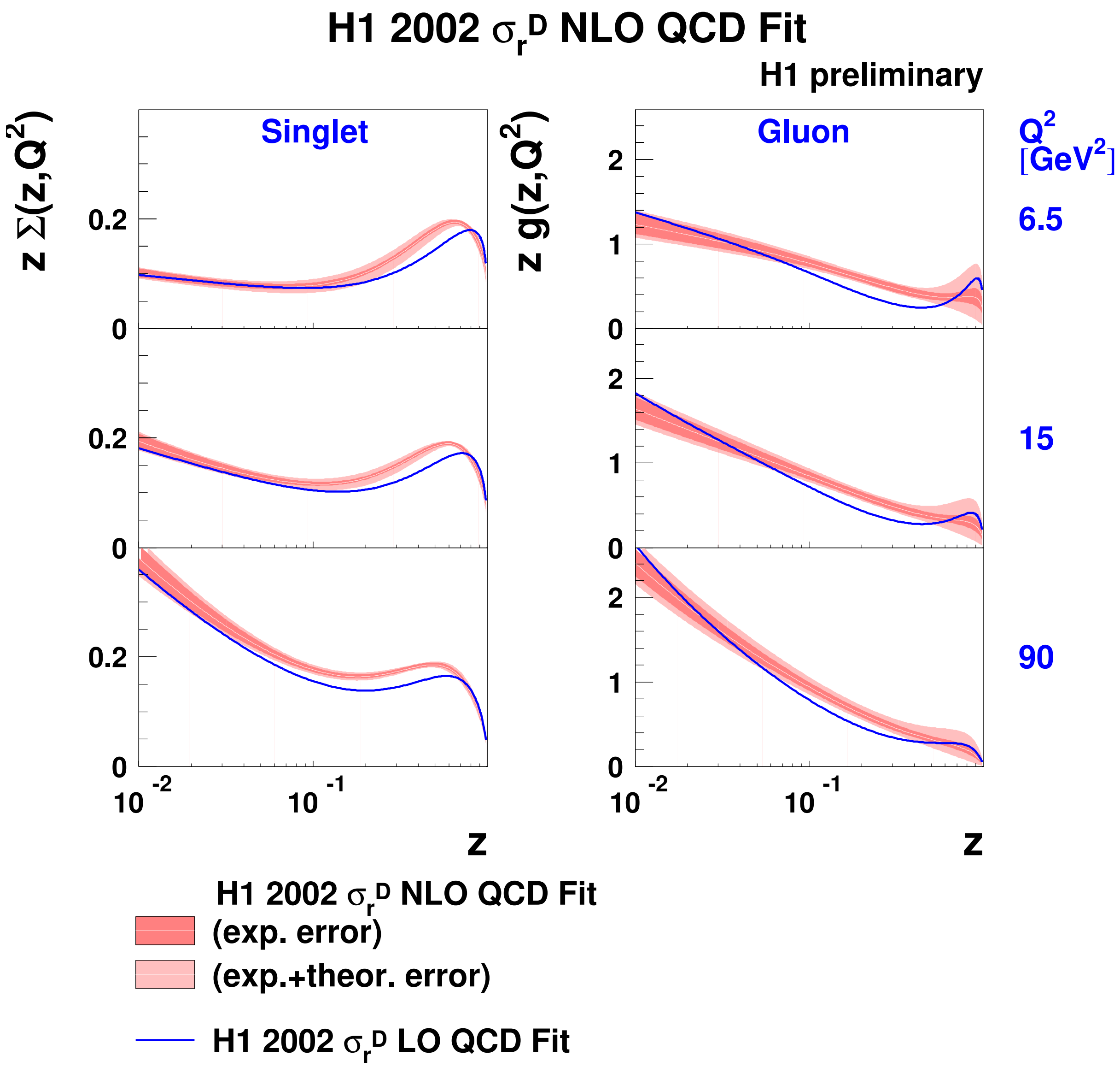

Figure 19: The same as figure 18 , but on a logarithmic z scale.

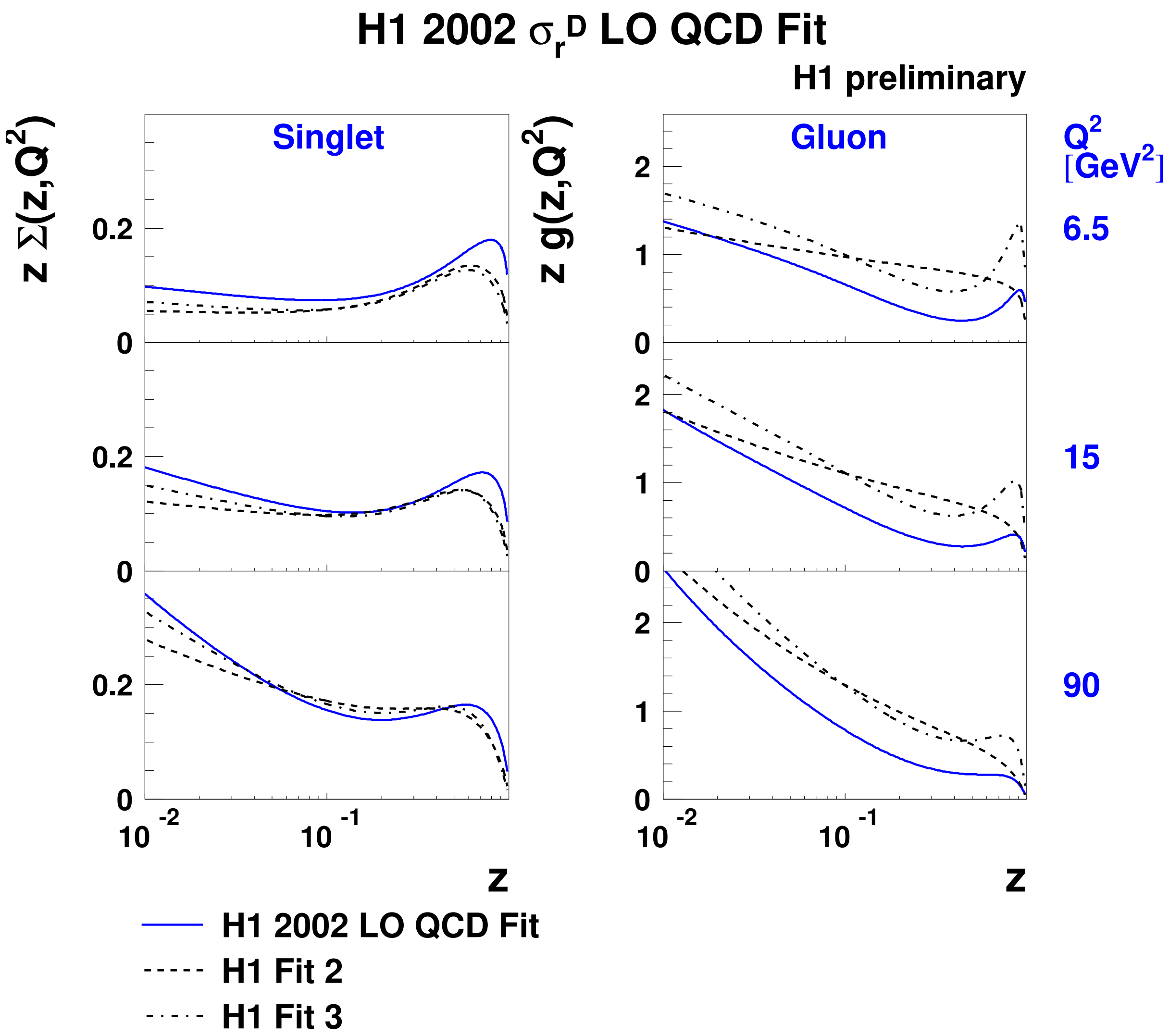

Figure 20: Comparison of the central values of the parton densities from the LO fit compared with the results of the two fits including glouns at the starting scale made to the 1994 H1 data [6]. The agreement in the singlet quark density is reasonable for $z < 0.65$ as used in the fits. The shape of the gluon is fairly similar to 1994 fit 3 ('peaked' gluon), except that the peak at highest z is significnatly smaller. The normalisation of the gluon is different by about 30% for low-medium z, a difference which would be inside the combined errors on the two extractions.

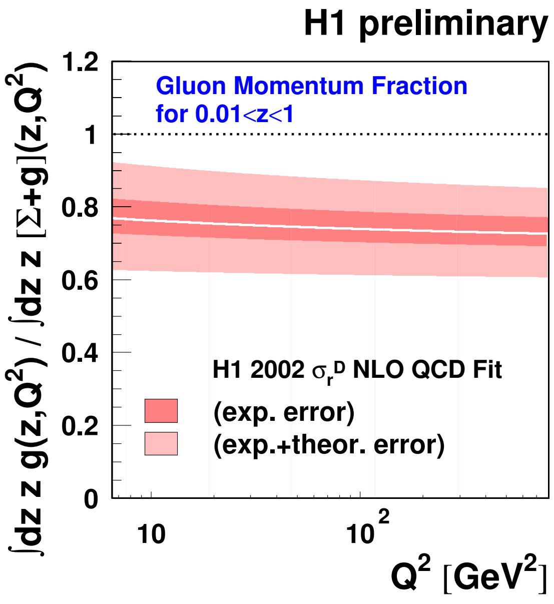

Figure 21: The fraction of the overall exchanged ('pomeron') momentum carried by gluons in the NLO fits, integrated over the z range measured and shown as a function of Q^2. The error bands again reflect the experimental (inner) and combined experimental and theoretical (outer) uncertainties. The result is fully consistent with that quoted in [6].

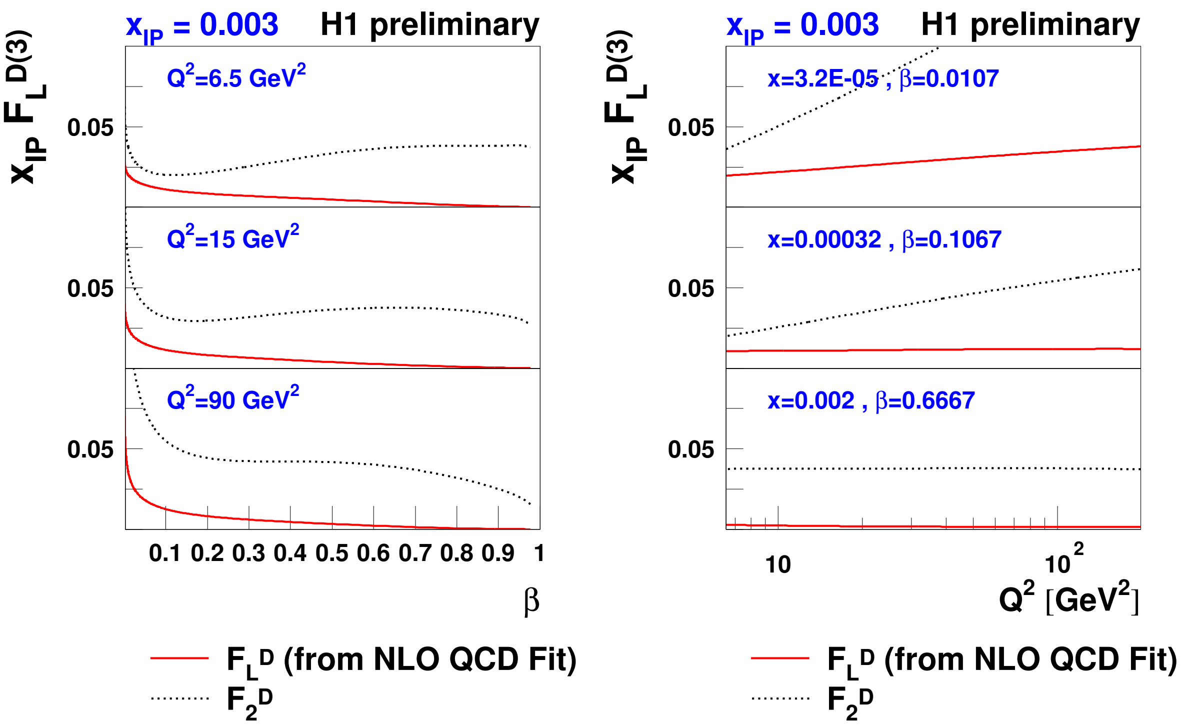

Figure 22: The leading twist component of F_L^D as obtained from the NLO QCD fit compared with its maximum possible value of F_2^D. The values of F_L^D are comparatively large, since they are closely related to the (dominant) gluon density at NLO.

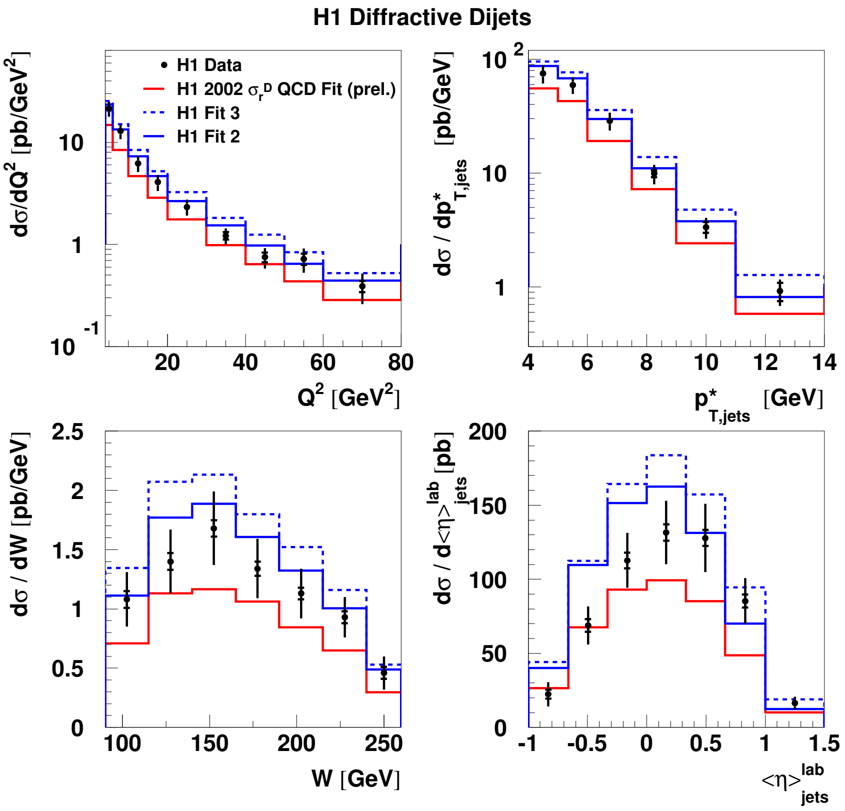

Figure 23: H1 measurements of diffractive dijets [7] compared with the new and old ([6]) LO QCD fits with the same assumptions for the Monte Carlo modelling as in [7]. The dijet cross sections differential in Q^2, the jet transverse momentum in the $\gamma^* p$ centre of mass frame ($p^*_{\mathrm{T,jets}}$), W and the jet pseudorapidity in the laboratory frame ($\langle\eta\rangle^{\mathrm{lab}}_{\mathrm{jets}}$) are shown. Accounting for the uncertainties in the parton densities, for modelling uncertainties such as the choice of renormalisation / factorisation scales and for higher order QCD effects, the overall normalisation difference between data and the new fits is probably not surprising. The shapes of the distributions remain well described.

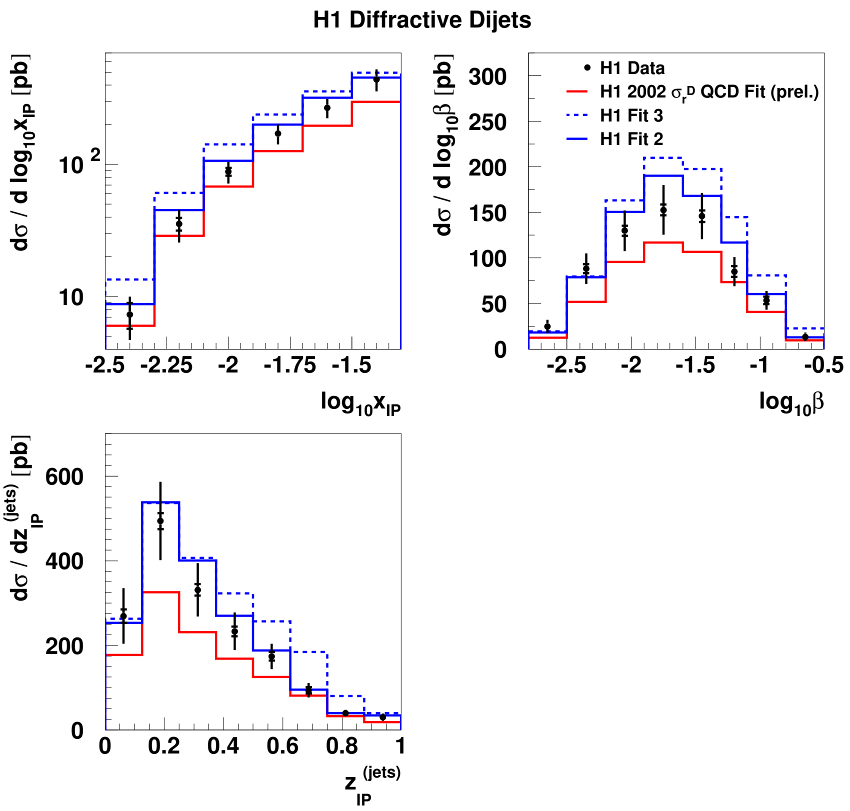

Figure 24: H1 measurements [7] of diffractive dijet cross sections differential in the diffractive variables $\log x_{I\!P}$, $\log \beta$ and the fraction $z_{I\!P}^{\rm jets}$ of the exchanged momentum transferred to the dijet system, compared with the new and old ([6]) LO QCD fits with the same assumptions for the Monte Carlo modelling as in [7].

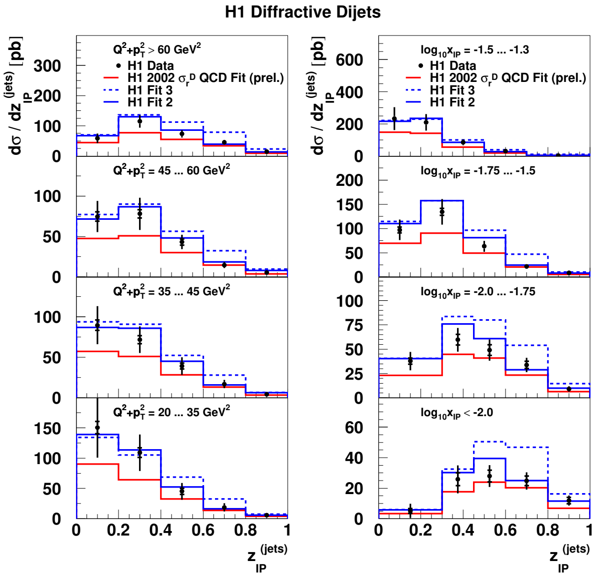

Figure 25: H1 measurements [7] of diffractive dijet cross sections as a function of $z_{\mathbb{P}}^{\rm jets}$ in different intervals of $Q^2 + p_{\rm T,jets}^{*\,2}$ and of $x_{\mathbb{P}}$, compared with the new and old ([6]) LO QCD fits with the same assumptions for the Monte Carlo modelling as in [7].

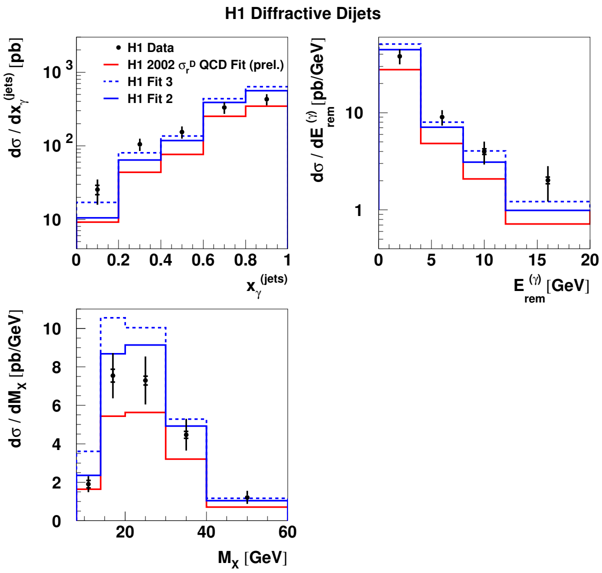

Figure 26: H1 measurements [7] of diffractive dijet cross sections differential in the fraction $x_\gamma^{\rm jets}$ of the virtual photon momentum transferred to the dijet system, the energy $E_{\rm rem}^{\gamma}$ in the photon hemisphere reconstructed outside the jets and $M_{\rm X}$, compared with the new and old ([6]) LO QCD fits with the same assumptions for the Monte Carlo modelling as in [7].

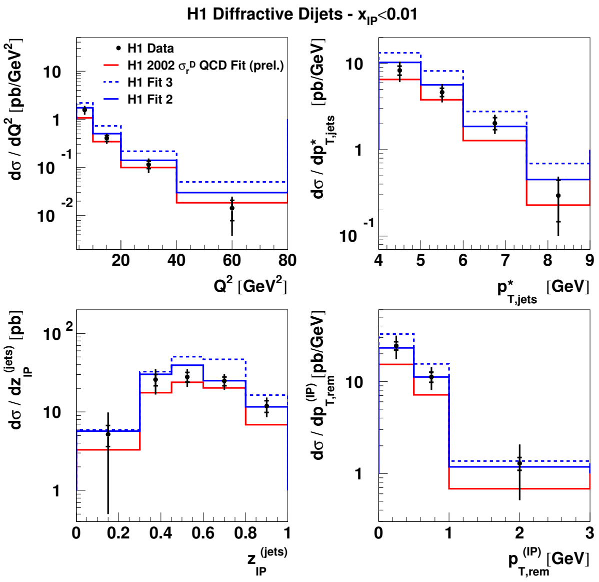

Figure 27: H1 measurements [7] of diffractive dijet cross sections in the restricted region $x_{I\!P} < 0.01$, compared with the new and old ([6]) LO QCD fits with the same assumptions for the Monte Carlo modelling as in [7]. The cross sections are shown differentially in Q^2, $p^*_{\mathrm{T,jets}}$, $z^{\mathrm{jets}}_{I\!P}$ and the transverse momentum $p^{I\!P}_{\mathrm{T,rem}}$ in the 'pomeron' hemisphere reconstructed outside the jets.

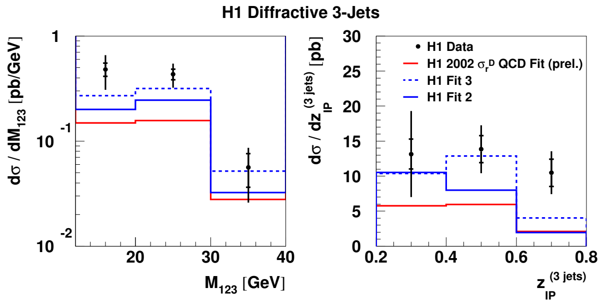

Figure 28: H1 measurements [7] of diffractive three-jet cross sections compared with the new and old ([6]) LO QCD fits with the same assumptions for the Monte Carlo modelling as in DESY-00-174. The cross sections are shown differentially in the three jet invariant mass M_{123} and in the fraction of the exchanged momentum transferred to the three-jet system $z^{\mathrm{3jets}}_{I\!P}$.

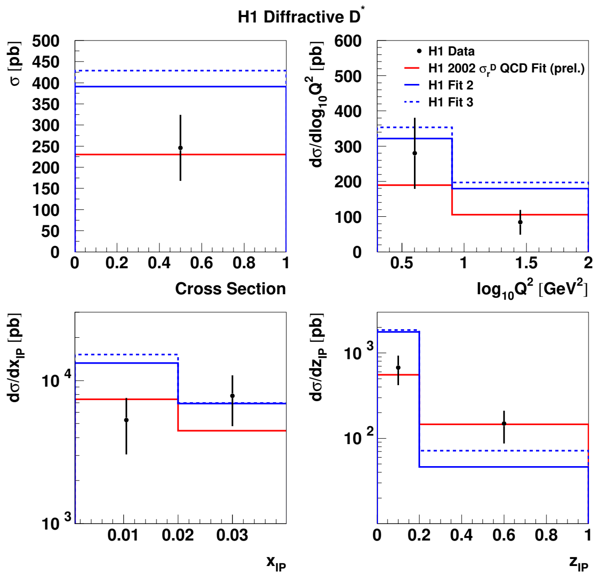

Figure 29: H1 measurements [8] of diffractive D^* production cross sections compared with the new and old ([6]) LO QCD fits with the same assumptions for the Monte Carlo modelling as in [8]. The cross section is shown integrated over the full measured phase space and differentially in $\log Q^2$, $x_{I\!P}$ and an estimator of the incoming gluon momentum fraction, $z_{I\!P}$. The overall cross section predicted in the new fits is in very good agreement with the dtaa, though the modelling is subject to the same uncertainties as for the dijet cross sections. The shapes of the differential distributions are well described.

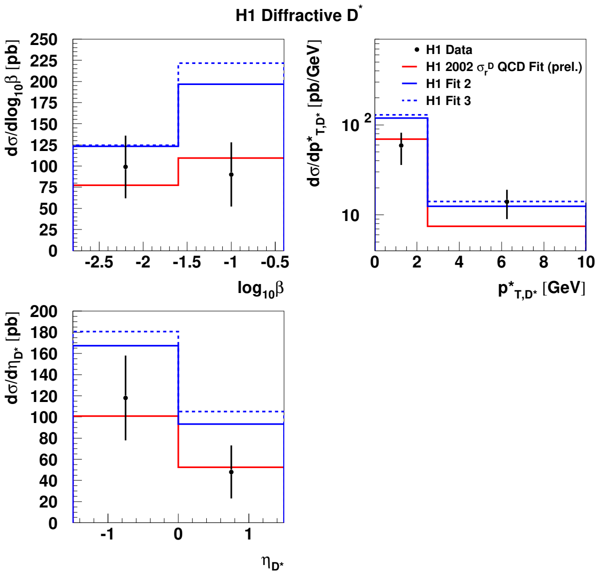

Figure 30: H1 measurements [8] of diffractive D^* cross sections differential in $\log\beta$, the D^* transverse momentum in the $\gamma^* p$ centre of mass frame ($p^*_{\mathrm{T,D^*}}$) and the D^* pseudorapidity in the laboratory frame η_{D^*}. The results are compared with the new and old ([6]) LO QCD fits with the same assumptions for the Monte Carlo modelling as in [8].

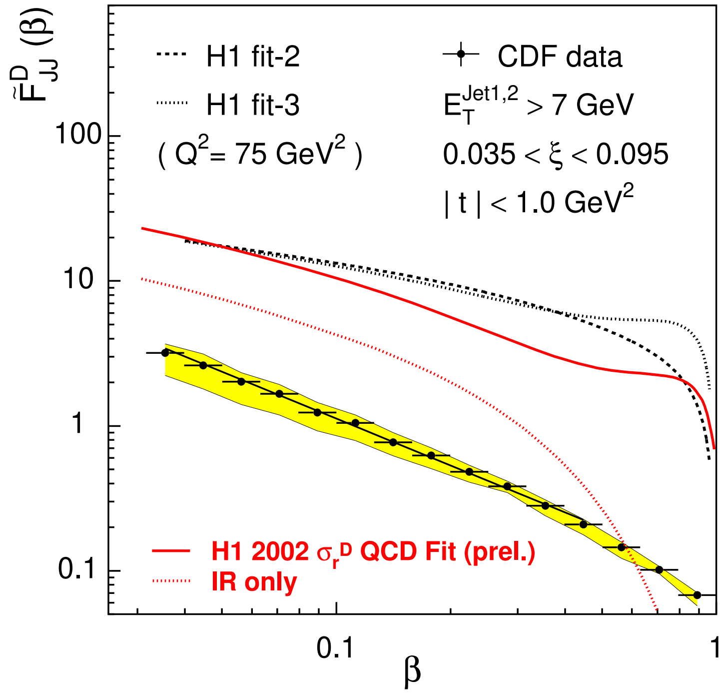

Figure 31: The quantity $\tilde{F}^{D}_{JJ}(\beta)$ as extracted from diffractive dijet data by the CDF collaboration [9], compared with the predictions of the new and old ([6]) LO QCD fits. Assuming Regge and QCD hard scattering factorisation, $\tilde{F}^{D}_{JJ}(\beta)$ corresponds to a convolution of the 'pomeron' (and sub-leading exchange) parton densities with the appropriate flux factors. The QCD hard scattering factorisation theorem is know to be invalid for diffractive hadron-hadron scattering. The new fits are slightly closer to the data at large β, but a large discrepancy of approximately one order of magnitude remains. This is often interpreted as being due to the destruction of rapidity gaps due to spectator interactions (absorptive corrections). In contrast to the comparison with the fits to 1994 data, the rapidity gap survival probability appears to be approximately constant over most of the β range. The predicted contribution of sub-leading exchanges is approximately 50% at low β, somewhat smaller than that from the 1994 fits.